Study of Nanoscale Friction under Ambient Conditions

by

© *Sajjad Salimi Nanehkarani*

A thesis submitted to the

School of Graduate Studies

in partial fulfilment of the

requirements for the degree of

Master of *Science*

Department of Physics and Physical Oceanography

Memorial University of Newfoundland

January 2020

St. John's Newfoundland

Abstract

Macroscopic friction involves interaction between many asperities of two surfaces in contact. After the invention of an atomic force microscope (AFM), the physics of friction can be studied at a single-asperity level. While the majority of such studies are performed in ultrahigh vacuum (UHV), friction in ambient conditions is more relevant to our everyday life. In this thesis, the results of AFM friction measurements on amorphous glass and crystalline mica surfaces in ambient conditions are presented. AFM friction in ambient conditions is found to differ significantly from vacuum conditions. While in UHV, the motion of the AFM cantilever is of the stick-slip type, in ambient conditions, only steady sliding is observed. Furthermore, in UHV, the average friction force is known to increase logarithmically with the pulling velocity. In ambient, on the other hand, it may either increase or decrease with the puling velocity. These experimental findings strongly suggest that AFM friction in ambient conditions is produced by water bridges between the AFM tip and the surface. A version of the mechano-kinetic model (MKM) is developed, in which the water bridges can spontaneously be created and broken. The main difference between the MKM proposed in this thesis and the one existing in the literature is that we assume that a water bridge may slide along the surface, whereas in the standard MKM, it is rigidly coupled to the surface. The main motivation for this modification is that it suppresses the onset of the stick-slip motion, making the steady sliding the generic regime of motion at slow pulling. A simple analytical formula is obtained for the average friction force that reproduces the experimental results both qualitatively and quantitatively.

Acknowledgements

Foremost, I would like to express my sincere gratitude to my supervisors Dr. Mykhaylo Evstigneev and Dr. Luc Y. Beaulieu for the continuous support of my M.Sc study and research, for their patience, motivation, enthusiasm, and immense knowledge. Their guidance helped me through out of my research for both experiments and simulations I did in my project.

I also thank my parents who have always been beside me. I can not imagine without my parents' support I could not overcome all project's hardships. Thanks Mama and Baba.

Contents

List of Tables

List of Figures

Chapter 1

Introduction and Literature Review

1.1 Introduction

The laws of friction were first investigated by Leonardo da Vinci and documented in his lab book [6]. Later, the phenomenological laws of friction were rediscovered by Coulomb and Amontons as the following statements [7]:

- Friction force is independent of contact area
- Friction force is proportional to the normal load F_n
- Kinetic friction does not depend on pulling velocity and is smaller than static friction

This classical perspective of friction, which is known as the Coulomb Laws, is useful for the application of friction on macroscopic scales. At the microscopic scale,

friction stems from the interaction of the small asperities between the surfaces in contact. The more asperities in contact, the greater the magnitude of the friction between the surfaces.

It is of interest to investigate single-asperity interactions between two surfaces, since small scale (micro and nano scales) friction measurements can show different behaviors from macroscopic friction. The invention of the atomic force microscope in 1986 by Gerd Binning and his group opened the door to nanoscale friction research [8].

Since da Vinci's time, the study of friction has been limited to macroscopic scale observations with the theories relying on classical laws of physics. One of the central studies from this period (by Bowden and Tabor) was aimed at explaining the hydrodynamic nature of friction using Reynolds' steady-state equation of fluid films [9]. According to the authors, the real contact area comes frome the large number of small junctions, known as asperities, and the friction force was considered to be proportional to the actual area of contact and average lateral force per unit area. By considering the multiple asperities interacting with the surface, this model satisfied the Coulomb friction laws as outlined in the previous section. However, considering a single asperity which is the Hertzian model subject, results in the friction force proportional to the normal force raised to the power 3/2, $F_n^{2/3}$ [1]. This new result showed that at the micro scales, the friction force does not behave similar to the macro scales.

As is often the case, new technologies lead to new scientific theories and discoveries. After the invention of the atomic force microscopy (AFM) [8], the study of nanoscale friction produced significantly different results through new measurement techniques and modelings. The critical study of friction at the nanoscale friction stems from

work done by Mate *et al.* [10], which was the first experimental study of friction at the atomic scale by AFM (see Figure 1.1). The authors observed that not only was the friction force a non-linear function of the normal load (of the AFM tip on the sample), but that friction versus position showed a stick-slip behavior at normal loads higher than 2.5×10^{-5} N. In stick-slip behavior, the tip apex occupies a particular surface site. By pulling the cantilever base along the surface, the elastic force due to the torsional deformation of the cantilever increases to the point where it overcomes the force exerted by the surface potential. At this point, the tip slips to another lattice site, and this process repeats itself with the periodicity of lattice constant [10, 11]. Since then, technologies have been developed such as ultra-high vacuum (UHV) systems which provided better resolution from AFM measurements. Under UHV conditions, kinetic friction was measured with different pulling velocities indicating that friction is an increasing function of the natural logarithm of the pulling velocity [12].

Besides experimental approaches, various modeling approaches were also developed. The Prandtl-Tomlinson's (PT) model, originally introduced by L. Prandtl [13], is a basic model used to explain experimental results on the UHV nanofriction. In the PT model, the cantilever tip is modeled as a mass-spring system that moves along the surface as a result of a constant pulling velocity v. According to the PT model, there are several different forces which are exerted on the cantilever tip: the dissipative force also known as the damping force, the force due to the surface potential, the elastic force, and the force related to random noise due to thermal fluctuations. In this model, the tip is considered as a Brownian object and the Langevin equation describes the equation of motion of the tip as a stochastic motion [14]. The model successfully reproduces the main features of UHV nanofriction, in particular the stick-slip motion

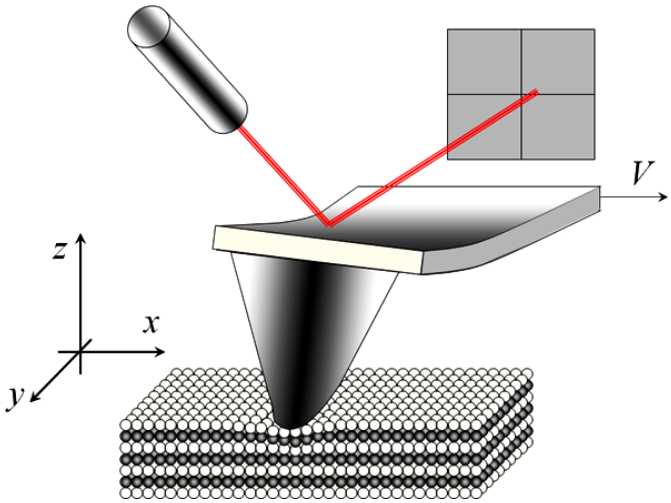

(a)

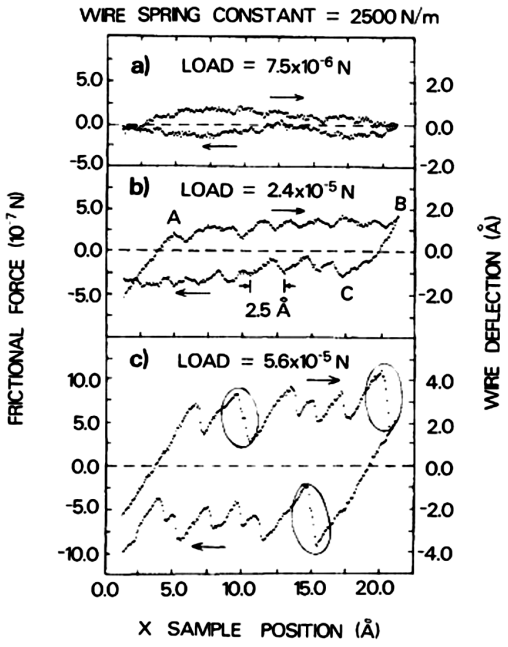

(b)

Figure 1.1: (a)A sketch of an AFM nanofriction experiment, in which the tip of an AFM is dragged along an atomically flat surface, and the resulting friction force is measured optically from the elastic deformation of the cantilever. (b) The friction force vs. cantilever base position at different normal loads from [1]

and the logarithmic velocity dependence of friction [15], although deviations from the model have also been reported [16].

Ultra-high vacuum rarely shows up in our everyday life; hence, a study of AFM friction in ambient conditions is just as important as UHV friction research. This research direction was initiated by Riedo et al. [17, 18]. It was immediately recognized that in ambient conditions, friction arises due to formation and rupture of capillary bridges [17, 18]. At about the same time, a Mechano-Kinetic (MK) model was introduced [19], which attributes friction to formation and rupture of multiple bonds between the tip and the surface. This model seems like an ideal one to describe friction in ambient conditions. Surprisingly, no direct comparison between the MK model and an AFM friction experiment in ambient conditions have been performed to our best knowledge. The purpose of this Thesis is to fill this gap.

Our study includes two parts, modeling, and experiment. In the next chapter, the MK model is introduced as formulated originally [19]. Because we never observed the stick-slip behaviour in the experiment, this MK model is modified in such a way that suppresses the stick-slip regime. An analytical expression for the mean friction force is derived in the experimentally relevant asymptotic limit of high cantilever stiffness. It is shown that our modified MK model may even exhibit Coulomb, i.e. velocity-independent, friction at the single-asperity level. In the third chapter, lateral force microscopy experiments are described and experimental results are provided in terms of the average friction versus velocity and normal load. After that, a comparison between experimental data and simulations is reported. Finally, our results are summarized.

Chapter 2

Mechano-kinetic (MK) model

2.1 The original MK model

The mechano-kinetic (MK) model was originally introduced by Filippov, Klafter, and Urbakh in 2004 [19]. Within this model, the AFM tip interacts with the substrate via many bonds, whose nature was not specified in the original publication [19]. In later publications, they were identified with capillary (water) bridges [20, 21]. The bonds are modeled as overdamped elastic springs, and their extension by an AFM tip results in a counterforce interpreted as friction. The mechanical part of the model describes the motion of the cantilever, the tip, and the extension of the water bridges, according to Newton's laws. The kinetic part of the model describes the formation and rupture of the bridges as random thermally activated processes. Here, we outline a simplified version of this model. Our simplifications will be clarified every time they are introduced. They do not affect the physics behind the model.

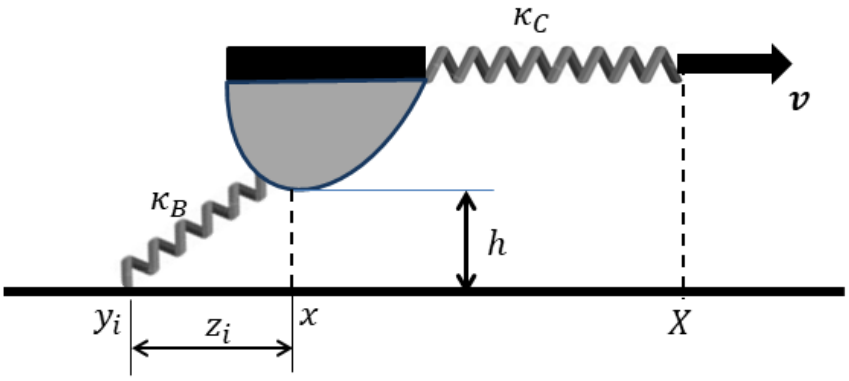

Figure 2.1: Schematic interaction of the apex of the cantilever tip with the surface.

2.1.1 Mechanical part

We model the cantilever as a spring of stiffness κ_C. Its one end represents the cantilever base, which is moving uniformly with the velocity V and has the coordinate

$$X = Vt \ . \tag{2.1}$$

The other end of this spring represents the cantilever tip apex with the coordinate x. The spring constant κ_C describes the effect of the torsional deformation of the cantilever beam and the tip. For more sense of MK model it would be useful to see the Figure 2.1. Its value is of the order of 1 N/m, as established experimentally [12]. The elastic force

$$f = \kappa_C(X - x) \tag{2.2}$$

equals the force of friction by Newton's third law.

The tip interacts with the surface via many water bridges. One end of each bridge, which we will call "the head", is attached to the tip apex and has the coordinate x. The other end, "the tail", is attached to the surface and has the coordinate y_i, where

the subscript i labels the bridges. Each bridge is modeled as an elastic spring with the spring constant κ_B. It produces the force

$$f_i = -\kappa_B z_i \tag{2.3}$$

on the cantilever tip. Here,

$$z_i = x - y_i \tag{2.4}$$

is the extension of the ith bridge.

The force expression (2.3) differs from the one used in [19] in that our formulation is completely one-dimensional, whereas in [19], the tip apex was assumed to be at some distance h from the substrate, and hence the bridge extension was $\sqrt{z_i^2 + h^2}$. Our formulation is a special case when $h = 0$.

We further assume that each bridge is an overdamped spring with the damping coefficient η_B so high that as long as at least one bridge exists between the tip and the substrate, the tip dynamics is heavily damped. We also assume that η_B is much higher than the damping coefficient of the cantilever itself. Denoting the number of active bridges, i.e. the ones that are formed between the tip and the substrate as N_{on} and the dynamics of the tip apex can then be expressed as an overdamped equation of motion

$$0 = -N_{on}\eta_B \dot{x} - \kappa_B \sum_i (x - y_i) + \kappa_C (X - x) \ . \tag{2.5}$$

It differs from the one adopted in [19] in several respects:

(i) In [19], the tip possesses inertia, and so the left-hand side of the equation of motion is not zero, but of the mass times acceleration form. This difference is not crucial, because in the work [19], no inertia-related effects have been reported.

(ii) The damping force on the cantilever is assumed to originate from direct tip-substrate interaction, and therefore it is independent on the number of bridges in [19].

(iii) A further difference between our model and [19] is in the way how we treat the bridges after they are broken. In [19], once a bridge is broken, it relaxes to equilibrium in an overdamped manner according to $z_i(t) \propto e^{-\lambda t}$, where λ is the relaxation constant in the notation of [19]. In contrast, we assume that after rupture, a bridge disappears, and new bridges are formed with the initial length set to zero. This difference should not play a role as long as the bridge formation rate ω_{on} is small compared to the relaxation rate λ.

(iv) Finally, in [19], the bridges that already exist are assumed to be in equilibrium all the time. This point is not quite consistent with the features (ii) and (iii) of the model [19]. It is hard to understand why the bridges act as overdamped springs only after they are broken, and when they are intact, they merely produce a force $-\kappa_B z_i$ independent on the extension speed $\dot{z}_i$. Such a "dual" nature of the bridges can hardly be justified physically. If bridge dynamics is overdamped after rupture, then one would expect that when the tip pulls an intact bridge apart, a dissipative force proportional to the bridge extension rate, $-\lambda \dot{z}_i$, should also emerge in the equation of motion for the tip. This force should also be proportional to N_{on} the number of active bridges. This force is present in our equation (2.5). It appears as the first term in the right-hand side of our equation of motion (2.5).

In principle, it is easy to introduce an additional damping force that is independent on the number of bridges in (2.5), tip inertia, and the internal dissipation of the tip. But all these modifications also mean introducing additional model parameters, whose values are not obvious. Therefore, we will consider the model (2.5) as the simplest,

minimalistic model of friction due to water bridges.

Admittedly, it does not reflect the full complexity of the tip dynamics. For instance, if there are no active bridges, the first two terms in the right-hand side of Eq. (2.5) are zero, implying that the tip apex immediately equilibrates to the elastic energy minimum $x = X$. The equations of motion (2.5) are, therefore, applicable when the water bridges are present. Fortunately, this is precisely the regime in which we are interested.

2.1.2 Kinetic part

The kinetic part of the model describes the formation and rupture of water bridges. It is assumed that there is a maximal number of bridges, N_B, that can be supported. Out of them, N_{on} bridges are active, allowing for $N_B - N_{on}$ more bridges to be formed. At the same time, the existing bridges may break. Bridge formation and rupture are random events. The probability of bridge formation/rupture per unit time are called the formation/rupture rates and are denoted as ω_{on} and ω_{off}.

We assume that the bridge formation rate depends on the tip velocity $\dot{x}$ relative to the substrate. The faster the tip moves, the smaller the bridge formation probability. We focus on the following model function:

$$\omega_{on}(\dot{x}) = \frac{\Omega_{on}}{\sqrt{1 + (\dot{x}/V_0)^2}} \ , \tag{2.6}$$

where Ω_{on} is the bridge formation rate when the tip is stationary, and V_0 is a characteristic velocity. Its magnitude should depend on the chemistry and morphology of the surface and the tip, relative humidity, and temperature. We will treat it as a fit parameter to be determined experimentally. This functional form emphasizes

the fact that ω_{on} depends only on the magnitude of the tip velocity, but not on its direction. Furthermore, at fast pulling $(\dot{x}/V_0) >> 1$, and we have $\omega_{on}(\dot{x}) \propto 1/|\dot{x}|$.

The bridge rupture rate is assumed to exponentially increase with the bridge extension z_i. The rationale behind this is that bridge rupture is a thermally activated process, whose probability per unit time is given by the Arrhenius law, $\omega_{off} = \Omega_{off} e^{-\Delta U/kT}$, where Ω_{off} is the rate of rupture of a newly formed bridge, ΔU is the energy barrier against rupture and kT is the thermal energy. A further assumption is that the energy barrier decreases with the bridge extension z_i approximately linearly (at least for small values of z_i), $\Delta U(z_i) \propto -\alpha|z_i|$, where α is the inverse characteristic length to be determined from fitting the experimental data,as first proposed in [22]. It leads to

$$\omega_{off}(z_i) = \Omega_{off} e^{\alpha|z_i|} \ . \tag{2.7}$$

More sophisticated expressions for $\Delta U(z_i)$ can also be considered, such as $\Delta U(z_i) = \Delta U(0)(1 - z_i/z_c)^{3/2}$ [19], where $\Delta U(0)$ is the energy barrier at zero extension, and z_c is the critical extension, at which the barrier disappears. These modifications introduce more parameters into the model, but do not alter its physics qualitatively. Therefore, we will stick to the simplest expression (2.7), which contains only two model parameters, Ω_{off} and a characteristic length against rupture α^{-1}.

2.1.3 Simulation details

Time is discretized into discrete steps of small magnitude Δt, that is, $t_n = n\Delta t$. At the nth step, the tip position has the value x, the tip base position is at $X = Vt_n$, and there are N_{on} active bridges with extensions $z_i(t_n)$. These parameters are then

updated on the next time step as follows:

1. Rupture of the existing bridges. Consider an active bridge at the moment t_n. The probability of its survival over time Δt is governed by the rate equation

$$\dot{P}(t) = -\omega_{off}(z_i(t))P(t) \tag{2.8}$$

where $z_i(t)$ is the bridge extension at time t. With the initial condition $P_i(t_n) = 1$, the rate equation has the solution

$$P(t) = e^{-\int_{t_n}^{t} ds\, \omega(z_i(s))} \ . \tag{2.9}$$

Focusing on small time intervals Δt, the probability that the bridge will remain active at time $t_{n+1} = t_n + \Delta t$ can be approximated as

$$P_{off} = e^{-\omega_{off}(z_i(t_n))\Delta t} \ . \tag{2.10}$$

To simulate this random event, a random number uniformly distributed between 0 and 1 is generated, $r \in (0, 1)$. If this number turns out to be smaller than P, the bridge is left intact. If it turns out that $r > P_{off}$, the active bridge is ruptured. This procedure is applied to all bridges that are active at time t_n.

2. Formation of the new bridges. Similarly, $P_{on} = e^{-\omega_{on}(v)\Delta t}$ represents the probability that a new bridge will be formed where $v = dx/dt$ is the velocity of the tip relative to the substrate. Again, a random number $r \in (0, 1)$ is generated, and if $r < P_{on}$, a bridge is formed with the tail coordinate set to x and extension set to 0. This procedure is performed $N_B - N_{on}$ times.

3. The number of active bridges, N_{on}, is updated. This is done by assigning to each bridge a Boolean variable q_i, $i = 1 \ldots N_B$, such that $q_i = 1$ if the ith bridge is

on and $q_i = 0$ if it is off. Whenever a bridge is broken in step 1, the corresponding q_i is set to 0; and whenever a new bridge is formed in step 2, the corresponding q_i is set to 1. Then, $N_{on} = \sum_{i=1}^{N_B} q_i$. This concludes the kinetic part of the time step.

4. The cantilever base position X is then shifted by the amount $V\Delta t$.

5. If there are no active bridges, the tip position x is set to X and its velocity v is set to the pulling velocity V.

6. Otherwise, the tip velocity is calculated according to Eq. (2.5), and the tip position is changed by the amount $\dot{x}\Delta t$. The value of $v \equiv \dot{x}$ obtained here is to be used in step 2.

2.2 MK model with mobile water bridges

There is both experimental [23–25] and computational [26] evidence that under ambient conditions with relative humidity of at least 15 %, a hydrophilic surface is covered with a few monolayers of water. This means that water bridges are formed not between the tip and the substrate, but between the tip and a thin water layer that covers the surface. While in the original version of the model [19], the tail of the water bridge was assumed to be rigidly pinned to a particular surface site, there is no reason to believe that such pinning sites may exist on a water-covered surface.

Therefore, we introduce a crucial modification into the model by assuming that the tails of the bridges are mobile. Their motion is expected to be associated with a damping force proportional to the bridge tail velocity, with the proportionality constant being the surface damping coefficient η_S. Because now the bridge tails are mobile, their coordinates y_i are functions of time. Hence, the damping force in the

tip equation of motion (2.5) should be proportional to the tip velocity relative to the bridge tails, leading to the modification

$$0 = -\eta_B \sum_i (\dot{x} - \dot{y}_i) - \kappa_B \sum_i (x - y_i) + \kappa_C (X - x) \ . \tag{2.11}$$

We furthermore need an equation for the dynamics of an ith bridge tail. Assuming overdamped limit, this equation reads

$$0 = -\eta_S \dot{y}_i - \eta_B (\dot{y}_i - \dot{x}) - \kappa_B (y_i - x) \ . \tag{2.12}$$

In the limit $\eta_S \to \infty$, the latter equation gives $\dot{y}_i \to 0$, and bridges become immobilized; then, Eq. (2.11) becomes equivalent to the original Eq. (2.5).

Eqs. (2.11), (2.12) are not suitable for numerical simulations, because they mix the velocities of all the degrees of freedom involved. For numerical simulations, it is desirable to express the rate of change of each coordinate in terms of the coordinates only. Fortunately, this is easily done. Taking the sum of Eq. (2.12) over all active bridges, $(\eta_S + \eta_B) \sum \dot{y}_i = \eta_B N_{on} \dot{x} - \kappa_B \sum (y_i - x)$, and plugging it in into Eq. (2.11), we obtain

$$N_{on} \frac{\eta_B \eta_S}{\eta_B + \eta_S} \dot{x} = -\kappa_C (x - X) - \frac{\eta_S}{\eta_B + \eta_S} \kappa_B \sum_i (x - y_i) \ . \tag{2.13}$$

Substitution of this expression for $\dot{x}$ into Eq. (2.12) gives

$$(\eta_S + \eta_B) \dot{y}_i = -\frac{\kappa_C}{N_{on}} \left(1 + \frac{\eta_B}{\eta_S} \right) (x - X) - \kappa_B \left(y_i - \frac{1}{N_{on}} \sum_j y_j \right) \ . \tag{2.14}$$

Numerical implementation of these dynamic expressions is the same as described above, except in step 6, Eq. (2.13) is used for the velocity, and a further step is added, namely:

7. Tip tail velocities are calculated according to Eq. (2.14) and their positions are incremented by $\dot{y}_i \Delta t$.

The maximal number of bridges:	$N_B = 1000$
Cantilever spring constant:	$\kappa_C = 1\,\mathrm{N/m}$
Bridge spring constant:	$\kappa_B = 0.01\,\mathrm{N/m}$
Bridge and surface damping coefficients:	$\eta_B = \eta_S = 0.01\,\mathrm{nN/(nm/ms)}$
On and off rate prefactors, Eqs. (2.6), (2.7):	$\Omega_{on} = \Omega_{off} = 10\,\mathrm{ms}^{-1}$
Characteristic velocity in the on-rate (2.6):	$V_0 = 1\,\mathrm{nm/ms}$
Characteristic length in the off-rate (2.7):	$\alpha^{-1} = 1$ nm

Table 2.1: Parameter values used in the simulations

2.3 Comparison of the MK model with mobile and stationary bridges: Friction regimes

For numerical simulations, we focus on the parameter values presented in Table 2.1. Initially, the cantilever base and the tip are assumed to be at the position $X = x = 0$, and the number of bridges corresponds to the stationary value $N_{on}(t = 0) = N_B\Omega_{on}/(\Omega_{on} + \Omega_{off})$. All these bridges were assumed to have zero extension. After that, the tip base starts to move at constant velocity V. Figure 2.2 shows the temporal evolution of the friction force [panels (a), (c), and (e)] and the number of active bridges [panels (b), (d), and (f)] within the original MK model (black curves) and the modified MK model (red curves).

At slow pulling, $V = 1\,\mathrm{nm/ms}$, both models exhibit steady sliding, in which friction force performs small fluctuations around the mean value, and the number of bridges fluctuates around the value, which is smaller than the equilibrium value of

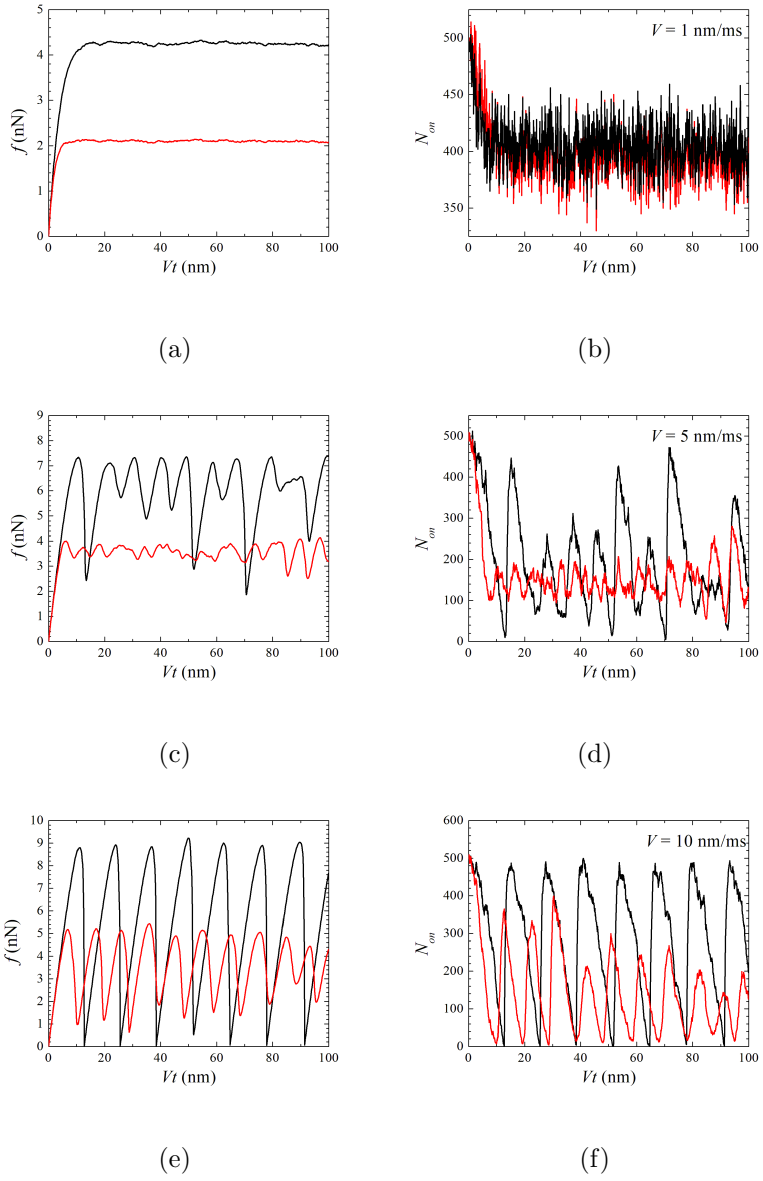

Figure 2.2: Evolution of the friction force (left panel) and the number of active bridges (right panel), as obtained from the simulations of the original MK model (black) and the MK model with mobile bridges (red) for (a,b) $V = 1\,\mathrm{nm/ms}$, (c,d) $V = 5\,\mathrm{nm/ms}$, and (e,f) $V = 10\,\mathrm{nm/ms}$.

$N_B\Omega_{on}/(\Omega_{on}+\Omega_{off})$.

Increasing pulling velocity to 5 nm/ms (Figure 2.2(b)) results in an onset of the stick-slip regime, which is much more pronounced in the original MK model than in our modified MK model. This is better visible in the fluctuations of the number of active bridges (right panel), which shows sawtooth-like oscillations in the simulations of the original MK model (black curve). The character of the bridge number fluctuations within our modified MK model at faster pulling velocity $V = 5$ nm/ms differs from the fast fluctuations observed at slower pulling at 1 nm/ms, cf. Figs. 2.2(a) and (b), right panel. But in contrast to the original MK model, the stick-slip regime is not quite developed in the modified MK model at $V = 5$ nm/ms. In particular, the friction force at this pulling velocity exhibits larger fluctuations around the mean value, but no sign of the sawtooth-like oscillations characteristic of the stick-slip motion.

The stick-slip regime fully develops at the pulling velocity $V = 10$ nm/ms for both models, see Figure 2.2(c). In this regime, the force evolves in time in a characteristic sawtooth-like pattern, consisting of the stick phases and sudden slips. The origin of this behavior is as follows. In a stick phase, the tip apex is bound to the surface by many bridges, and therefore it either practically does not move relative to the surface (original MK model), or its motion is much slower than the motion of the cantilever base (modified MK model). At the same time, pulling of the cantilever base results in an approximately linear increase of the elastic force f, resulting in a higher bridge rupture rate. Therefore, the number of active bridges continuously decreases.

Subsequently, the tip moves together with the cantilever with the velocity V. This motion, however, is very short-lived, because new bridges start to get formed. As the new bridges appear, the tip slows down, which increases the bridge formation rate

$\omega_{on}(\dot{x})$. This results in an even higher number of bridges, and in further slowing down of the tip. The number of active bridges reaches its maximum very quickly, and a new stick phase begins.

Why is the stick-slip regime stable at fast pulling, whereas the steady sliding is stable at slow pulling? Qualitatively, the reason is as follows. In order for the cantilever to slip, all or almost all active bonds must break. At slow pulling, rupture of a few active bonds does not mean that all bonds will break, because new bonds form too fast for this to happen. At fast pulling, on the other hand, the loading rate is too high for the surviving bonds to be able to stay attached to the tip indefinitely long.

The conclusion that we can make from this comparison between the original and the modified MK model is that depending on the pulling velocity V, two friction regimes are realized. At low pulling velocity, tip motion proceeds as a steady sliding, whereas at high pulling velocity, the tip exhibits stick-slip behavior. There is a critical velocity, V_c, which separates the two regimes. This critical velocity has a much lower value within the original MK model than within our modified MK model with mobile bridges. At some point, the last bridge breaks, and the tip quickly slides to a new equilibrium position $x = X$, minimizing the elastic energy. In the modified MK model, this slip event is possible even when a small number of bridges remain active; the tip simply drags those residual bridges to a new equilibrium position. It is for this reason that the force drops to zero in the original MK model, but remains finite in the modified MK model.

2.4 Stiff cantilever limit

2.4.1 Friction force

The model (2.13), (2.14) can be solved analytically in the limit of cantilever stiffness much greater than the bridge stiffness, in which case formation and rupture of bridges has little effect on the cantilever tip velocity. Hence, fluctuations of the tip velocity can be neglected, i.e. the tip moves with the same velocity V at which the cantilever base is pulled:

$$\kappa_C \gg \kappa_B \ , \quad \dot{x} = V \ . \tag{2.15}$$

In this limit, we first find the distribution of bridge extensions $z = x - y_i$. It follows from Eq. (2.12) that the extension of ith bridge is governed by the differential equation

$$(\eta_B + \eta_S)\dot{z} = \eta_S V - \kappa_B z \ . \tag{2.16}$$

Let us measure the time t from the moment of ith bridge formation, i.e. $z(0) = 0$. Then, the extension at any later time is given by

$$z(t) = z_{max}\left(1 - e^{-t/\tau}\right) \ , \quad z_{max} = \frac{\eta_S V}{\kappa_B} \ , \quad \tau = \frac{\eta_S + \eta_B}{\kappa_B} \ . \tag{2.17}$$

The important difference between the original and our version of the MK model is that in the original model, a bridge is extended uniformly with the velocity V, $z_i = Vt$. In our model, there is a velocity-dependent maximal length, z_{max}, which is reached with the characteristic extension time τ. After reaching this maximum, the bridge continues to move together with the cantilever without being extended further. The bridge extension rate is time-dependent:

$$u(t) \equiv \dot{z}(t) = \frac{1}{\tau} e^{-t/\tau} \ . \tag{2.18}$$

A bridge of extension z changes its length with the velocity

$$u(z) = \frac{z_{max} - z}{\tau} \ . \tag{2.19}$$

Let us find the probability $P(z)$ for a bridge to survive to the length z. In the time domain, bridge survival probability is governed by Eq. (2.8). Transforming Eq. (2.8) from the time to the extension domain according to Eq. (2.17), we have:

$$u(z)\frac{dP(z)}{dz} = -\omega_{off}(z)P(z) \ . \tag{2.20}$$

With the initial condition $P(0) = 1$, the bridge survival probability is found as

$$P(z) = \exp\left(-\int_0^z dz' \, \frac{\omega_{off}(z')}{u(z')}\right) \ . \tag{2.21}$$

For the off-rate given by Eq. (2.7), the integral can be expressed in terms of the exponential integral

$$E_1(x) = \int_x^\infty dt \, \frac{e^{-t}}{t} \tag{2.22}$$

as

$$\int_0^z dz' \frac{\omega_{off}(z')}{u(z')} = \tau\omega_{off}(z_{max}) \left[E_1\left(\alpha(z_{max} - z)\right) - E_1(\alpha z_{max})\right] \ . \tag{2.23}$$

Let $n(z,t)$ be the concentration of bridges of length z at time t, i.e. the number of bridges with length in an interval $(z, z+dz)$ is $n(z,t)\,dz$. The bridge concentration changes in time, because bridges enter and leave this interval due to pulling, and because bridges of length between z and $z + dz$ break with the rate $\omega_{off}(z)$. These statements are expressed in as a continuity equation:

$$\frac{\partial n(z,t)}{\partial t} = -\frac{\partial[n(z,t)u(z)]}{\partial z} - \omega_{off}(z)n(z,t) \ . \tag{2.24}$$

We are interested in the steady-state solution of this equation, $n(z) \equiv \lim_{t\to\infty} n(z,t)$, in which $\partial n/\partial t = 0$. This solution reads:

$$n(z) = C\,\frac{P(z)}{u(z)}\ . \tag{2.25}$$

The prefactor C can be found from the balance condition: In the steady state, the total number of bridge formation formation events per unit time, $(dN/dt)_+$, equals the total number of bridge rupture events, $(dN/dt)_-$. On average, there are

$$\langle N_{on}\rangle = \int_0^{z_{max}} dz\, n(z) \tag{2.26}$$

active bridges. Given that the maximal number of bridges that can be supported by the tip-substrate contact is N_B, the rate of increase of the bridge number is

$$\left(\frac{dN}{dt}\right)_+ = \omega_{on}(V)(N_B - \langle N_{on}\rangle)\ . \tag{2.27}$$

The number of bridge rupture events per unit time is

$$\left(\frac{dN}{dt}\right)_- = \int_0^{z_{max}} dz\,\omega_{off}(z)\,n(z)\ . \tag{2.28}$$

Equating $(dN/dt)_+ = (dN/dt)_-$, we obtain:

$$C = N_B \frac{\omega_{on}(V)}{\int_0^{z_{max}} dz \frac{P(z)}{u(z)}\left(\omega_{on}(V) + \omega_{off}(z)\right)}\ . \tag{2.29}$$

Once $n(z)$ is found, we can find the friction force

$$\langle f\rangle = \kappa_C\langle X - x\rangle \tag{2.30}$$

by averaging Eq. (2.13):

$$\langle f\rangle = \langle N_{on}\rangle\frac{\eta_B\eta_S}{\eta_B+\eta_S}V + \frac{\eta_S}{\eta_B+\eta_S}\kappa_B\langle N_{on}\rangle\langle z\rangle\ , \tag{2.31}$$

where

$$\langle z \rangle = \frac{1}{\langle N_{on} \rangle} \int_0^{z_{max}} dz\, z\, n(z) \tag{2.32}$$

is the average bridge extension. The first term in Eq. (2.31) represents the damping contribution that arises due to the finite speed of the cantilever tip relative to the substrate, and the second term is the elastic force due to the bridge extension.

2.4.2 Validation of the analytical formulae

In order to be absolutely certain that the analytical formulae for $\langle f \rangle$ and $\langle N_{on} \rangle$ are correct, we compare them with the simulations of the MK model performed in the limit $\kappa_C \to \infty$. In this limit, the tip coordinate is (almost) equal to X, and its velocity is just $\dot{x} = V$. The instantaneous friction force (2.4), $f = -\kappa_C(x - X)$, is given by the expression which directly follows from Eq. (2.13):

$$f = \left(N_{on}\eta_B V + \kappa_B \sum_i (X - y_i) \right) \frac{\eta_S}{\eta_B + \eta_S} \ . \tag{2.33}$$

Finally, the tail coordinates dynamics is governed by the equation that follows from (2.14):

$$(\eta_S + \eta_B)\dot{y}_i = \left(1 + \frac{\eta_B}{\eta_S} \right) \frac{f}{N_{on}} - \kappa_B \left(y_i - \frac{1}{N_{on}} \sum_j y_j \right) \ . \tag{2.34}$$

Shown in Fig. 2.3 is a comparison between the average friction force and the number of bridges obtained from simulations (black curves) and analytically (red curves), with all parameters (except κ_C) given in Table 2.1. A perfect agreement between the two sets of data is obvious. In fact, the curves representing the average number of active bridges, Fig. 2.3(b), are practically indistinguishable from each other. With respect to the average friction, Fig. 2.3(a), the curve obtained from the

simulations exhibits small, but noticeable fluctuations, especially at faster pulling. These fluctuations can be traced back to the fluctuations in the bridge extension, $z_i = X - y_i$.

As expected, the average bridge number $\langle N_{on} \rangle$ monotonically decreases with pulling velocity. This is not surprising, in view of the fact that bridge formation rate $\omega_{on}(V)$ decreases with V, and bridge rupture rate $\omega_{off}(z)$ increases with the bridge extension, which, in turn, increases with the pulling velocity.

Interestingly, the average friction force in the stiff-cantilever limit is a non-monotonic function of the pulling velocity, see Fig. 2.3(a). This can be understood as follows. On the one hand, the friction produced by a single active bridge increases with the pulling velocity. This is so, because its average extension $x - \langle y_i \rangle$ increases with V, and because so does the damping force due to the substrate, $-\eta_S \dot{\langle} \dot{y}_i \rangle$. But, on the other hand, the total number of active bridges, $\langle N_{on} \rangle$, decreases with the pulling speed. The friction maximum results from the competition of these two effects.

2.4.3 Coulomb friction

It is quite surprising that nanoscale single-asperity friction is usually a function of pulling velocity, whereas macroscopic dry friction is velocity-independent, as noted by Coulomb's friction law. Because of this difference with respect to the velocity dependence, extension of nanoscale friction theories to macroscopic scale is not trivial. It should involve additional assumptions about, e.g., asperity size distribution, or the distribution of the interaction parameters between the asperities.

In this respect, a natural question arises: Under what conditions can a nanoscale

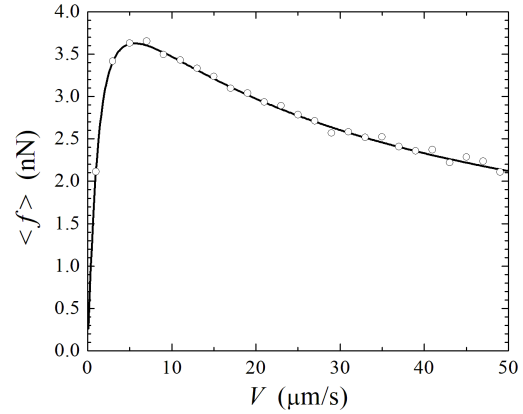

(a)

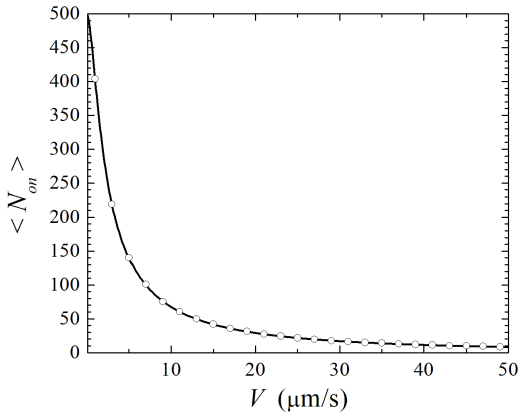

(b)

Figure 2.3: Velocity dependence of (a) the average friction force and (b) the average number of active bridges for the modified MK model with parameter values from Table 2.1 in the stiff-cantilever limit, $\kappa_C \to \infty$. Circles: numerical simulations, solid curves: analytical formulae (2.26) and (2.31).

friction model predict velocity-independent friction? Here, we show that within our

modified MK model, Coulomb friction is possible if the bond rupture rate is constant

$$\omega_{off}(z) = \text{const} \tag{2.35}$$

independent of the bridge extension, and if the condition (2.15) holds.

In this case, the analytical expressions obtained in the previous section can be simplified further. For the bridge survival probability, we obtain

$$P(z) = \exp\left(-\omega_{off}\tau \int_0^z \frac{dz'}{z_{max} - z}\right) = \left(1 - \frac{z}{z_{max}}\right)^{\omega_{off}\tau} \ . \tag{2.36}$$

Then, given that $\int_0^{z_{max}} dz P(z)/u(z) = 1/\omega_{off}$, we find the normalization constant from Eq. (2.29)

$$C = N_B \frac{\omega_{on}\omega_{off}}{\omega_{on} + \omega_{off}} \ . \tag{2.37}$$

Hence, bond length concentration is found as

$$n(z) = C\frac{P(z)}{u(z)} = N_B \frac{\omega_{on}\omega_{off}}{\omega_{on} + \omega_{off}} \tau \frac{(z_{max} - z)^{\omega_{off}\tau - 1}}{z_{max}^{\omega_{off}\tau}} \ , \tag{2.38}$$

the average number of active bridges is

$$\langle N_{on} \rangle = \int_0^{z_{max}} dz\, n(z) = N_B \frac{\omega_{on}}{\omega_{on} + \omega_{off}} \ , \tag{2.39}$$

and the average bridge extension is

$$\langle z \rangle = \frac{1}{\langle N_{on} \rangle} \int_0^{z_{max}} dz\, z\, n(z) = \frac{z_{max}}{\omega_{off}\tau + 1} \ . \tag{2.40}$$

Substitution of the last two expressions into the expression (2.31) for the friction force gives the friction force

$$\langle f \rangle = N_B \frac{\eta_S}{\eta_S + \eta_B} \frac{\omega_{on}}{\omega_{on} + \omega_{off}} \left(\frac{\kappa_B z_{max}}{\omega_{off}\tau + 1} + \eta_B V\right) \ . \tag{2.41}$$

Finally, using the expression (2.17) for z_{max}, we transform the average friction force to

$$\langle f \rangle = N_B \frac{\eta_S}{\eta_S + \eta_B} \frac{\omega_{on}}{\omega_{on} + \omega_{off}} V \left(\frac{\eta_S}{\omega_{off}\tau + 1} + \eta_B \right) \ . \tag{2.42}$$

Next, we assume that for fast pulling, the on-rate asymptotically decreases with velocity as

$$\omega_{on}(V) \propto \Omega_{on} \frac{V_0}{|V|} \ , \tag{2.43}$$

see Eq. (2.7). Then, the average friction force becomes

$$\langle f \rangle = N_B \frac{\eta_S}{\eta_S + \eta_B} \frac{\Omega_{on} V_0}{\omega_{off}} \left(\frac{\eta_S}{\omega_{off}\tau + 1} + \eta_B \right) \frac{V}{|V|} \ . \tag{2.44}$$

velocity-independent. Hence, within our model, Coulomb friction is explained as resulting from the interplay of two effects: an increase of the damping force that arises as a bridge is pulled over the surface, and a decrease of the average number of bridges with the pulling velocity.

2.5 Effect of cantilever stiffness on friction

It is instructive to see how the average friction force depends on the velocity for the parameter values from Table 2.1 at finite cantilever stiffness $\kappa_C = 1$ and to compare the results with the stiff-cantilever analytical approximations (2.26), (2.31). The results of this comparison are presented in Figure 2.4, showing (a) the average friction force and (b) the average number of active bridges, as obtained analytically (red curves) and numerically (black curves).

It is seen that for velocities below about 5 nm/ms, the analytical approximation is in perfect agreement with the numerical results, as the two curves are practi-

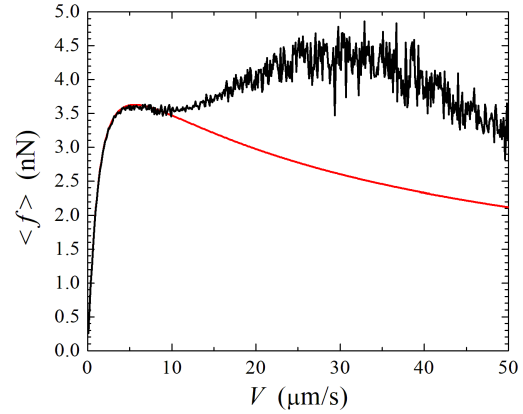

(a)

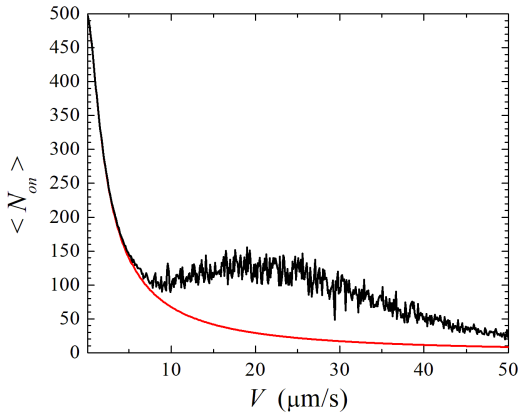

(b)

Figure 2.4: Velocity dependence of (a) the average friction force and (b) the average number of active bridges for the modified MK model with parameter values from Table 2.1. Black curves: numerical simulations, red curves: stiff-cantilever analytical approximations (2.26) and (2.31).

cally indistinguishable from each other. In this velocity range, the average friction force initially increases and then develops a maximum, whereas the number of active

bridges steadily decreases with the pulling velocity. This behaviour has already been discussed, see Section 2.4.2.

The stiff-cantilever approximation does not agree with the simulations at fast pulling, i.e. for V above 5 nm/ms. Interestingly, it is around this velocity that the steady-sliding regime is replaced by the stick-slip regime, see Figure 2.2. The inapplicability of the stiff-cantilever approximation in the stick-slip regime is due to the fact that this approximation is based on the assumption that the cantilever tip moves at a constant pulling velocity, $\dot{x} = V$. Obviously, this is not the case in the stick-slip regime, the tip velocity is very small in the stick phases and very high in the slip events.

It comes as a surprise that the velocity dependence of both friction force $\langle f \rangle$ and the number of active bridges $\langle N_{on} \rangle$ in the stick-slip regime is non-uniform. Both curves develop a maximum at slightly different velocities. The maximum of $\langle f \rangle$ occurs at $V \approx 30\,\mathrm{nm/ms}$, whereas $\langle N_{on} \rangle$ is maximized at $V \approx 20\,\mathrm{nm/ms}$.

The maximum of $\langle N_{on} \rangle$ can be explained as follows. In the stick phases, the tip velocity is much smaller than the pulling velocity V. Correspondingly, the bridge formation rate (2.6) is higher than the constant value $\omega_{on}(V)$ assumed in the stiff-cantilever approximation. Therefore, also the number of active bridges in a stick phase, N_{stick}, is higher than the stiff-cantilever value given by Eq. (2.26). During the stick-slip motion, the number of bridges oscillates between the value N_{stick} and almost zero, see Figure 2.2(c), and so the average number of bridges can be estimated as $N_{stick}/2$. This number may turn out to be higher than the stiff-cantilever approximation (2.26), i.e. after the onset of the stick-slip motion, $\langle N_{on} \rangle$ may increase with the pulling velocity V.

If the pulling velocity is too high, the elastic deformation of the bridges builds up too fast, implying a high bridge rupture rate $\omega_{off}(z)$, and hence a decrease of N_{stick} with V. The maximum in the $\langle N_{on} \rangle$ vs. V curve at around 20 nm/ms can be understood as a result of a competition between an enhancement of the bridge formation rate at slower pulling, and an increase of the bridge rupture rate at fast pulling.

Because the friction force is directly related to the number of the active bridges, it should also be maximized with the pulling velocity. The fact that the friction maximum is found at a slightly different pulling velocity than the maximum of $\langle N_{on} \rangle$ can also be understood. The value of $\langle f \rangle$ is determined not only by the number of the active bridges, $\langle N_{on} \rangle$, but also by the average bridge extension $\langle z \rangle$. The average extension of the friction bridges is monotonically increasing with the pulling velocity without any non-monotonicity. This effect makes the friction force to continue increasing even after reaching the velocity at which $\langle N_{on} \rangle$ is maximized. Eventually, the decrease of $\langle N_{on} \rangle$ with V dominates, resulting in a decrease of $\langle f \rangle$ with V at fast pulling. This implies that the friction force in the stick-slip regime is also a non-monotonic function of the pulling velocity, but the friction maximum occurs at a higher velocity than the maximum of the average number of active bridges.

Chapter 3

Experiments

In this chapter, we will discuss the instruments needed for performing friction force microscopy including calibration of the system, and the actual friction measurement operation. First, the atomic force microscopy (AFM), including a practical overview of how the AFM works and the underlying theory surrounding the instrument will be discussed. In the following, a brief introduction on how to set up the instrument for performing the measurement is provided. In section 3.3 a discussion of how to calibrate the instrument for performing both normal and lateral force microscopy is presented, and finally, the experimental results are provided in section 3.6.

3.1 Atomic Force Microscopy

The first Atomic Force Microscopy (AFM) was invented in 1986 by Gerd Binnig and Calvin Forrest Quate [8]. The atomic force microscope is an instrument used to measure the surface topography of materials and the interactions between the tip at the end of the cantilever and substrate for conductors, semiconductors, and insulators.

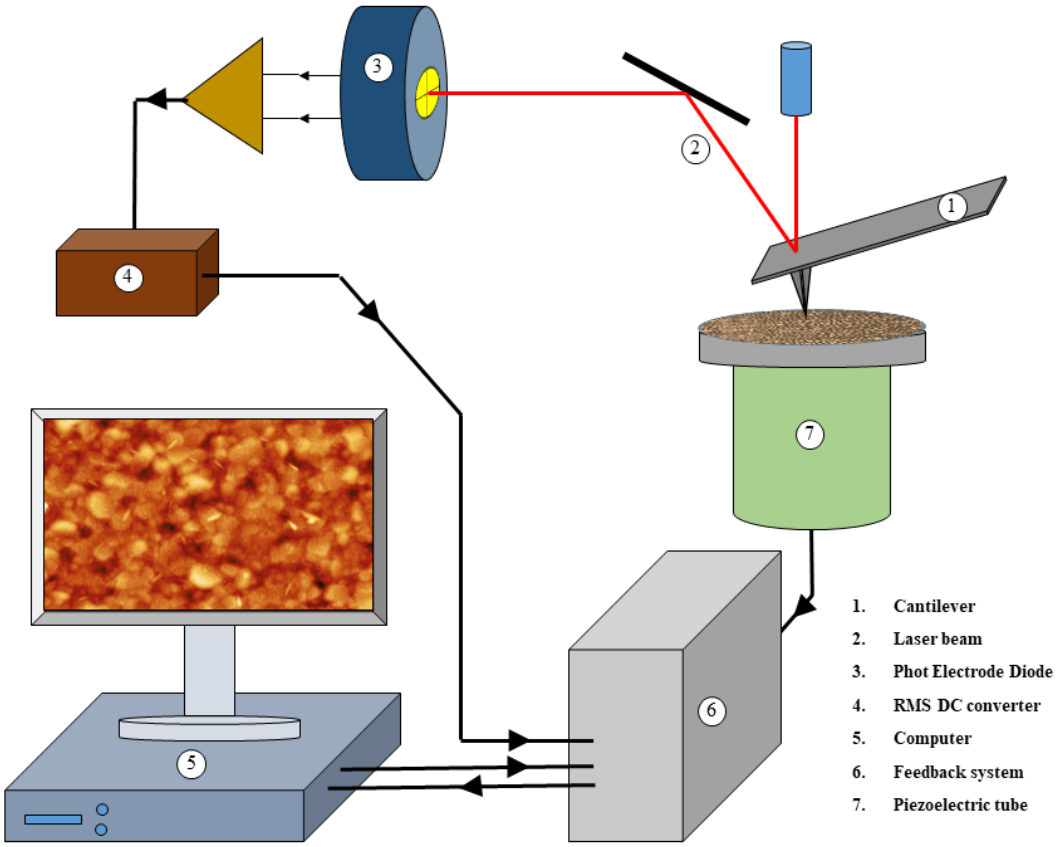

Figure 3.1: Main parts of a typical atomic force microscope.

The topography of a surface provides information about the size of the surface corrugations and the surface roughness. The resolution of this instrument relies on the size of the tip at the end of the cantilever. The smaller the size of the tip, the higher resolution, which provides more details from the image. The main parts of an AFM shown in Figure 3.1 are discussed below:

The probe

The probe consists of a rectangular cantilever (labeled (1) in Figure 3.1) with a

sharp tip at the free end as shown in Figure 3.2. The size of the cantilever is on the order of hundreds of micrometers, while the tip is a few micrometers in height. The geometry of the tip varies based on the type of measurement to be performed. In most cases, it is in the shape of tetrahedron, but depending on the topography and material of the substrate the shape of the tip could be changed. The AFM probes could be used for contact and non contact imaging modes as well as magnetic, electrical and biophysical measurements.

Optical Beam Deflection System

During the operation of the instrument the deflection and twisting of the cantilever is monitored using an optical beam deflection system (labeled (2,3) in Figure 3.1). The laser beam is made incident on the free end of the cantilever, reflected from the cantilever and detected by photosensitive detector (PSD). As shown in Figure 3.3, the PSD has four quadrants **A,B,C,** and **D**. When the cantilever deflects or twists, the position of the laser beam changes correspondingly and the detected photo-currents from the quadrants produces a voltage proportional to the intensity as $(I_A + I_B) - (I_C + I_D)$ or $(I_A + I_C) - (I_B + I_D)$ for a vertical or lateral deflection respectively.

Piezoelectric Tube and System Controller

During the imaging process, applying a force in the vertical z direction and moving the sample in x and y direction are done by the piezoelectric tube (labeled (7) in Figure 3.1). The piezoelectric tubes used in AFMs, are produced from Lead, Zirconium, and Titanate (PZT). Powder of each PZT component with different proportions is

sintered to form a poly-crystalline tube-shaped object. With each crystal having a specific dipole moment provides a large voltages across the material causes a net contracting elongation of the tube [27]. Controlling these processes requires a very precise controlling system. The feedback system (labeled (4,6) in Figure 3.1) is an interface between both the RMS DC converter and the PZT tube, which applies the control on detected voltage from one side and changing the length of the tube on the other side, regarding the optimized adjustment of the cantilever on top of the sample.

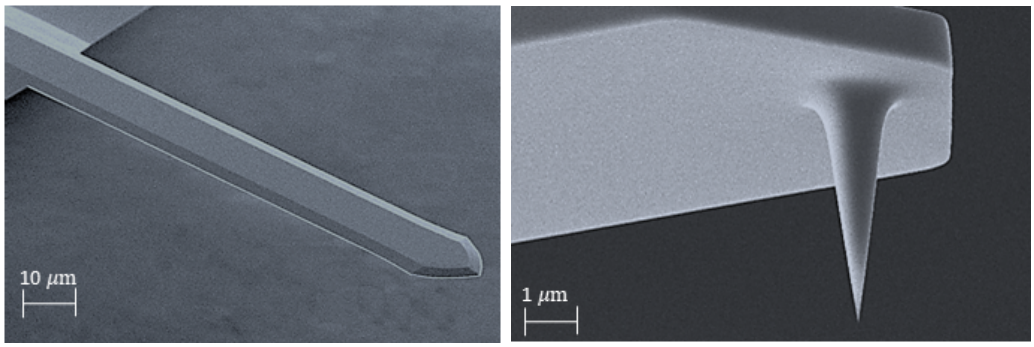

(a) (b)

Figure 3.2: SEM image of (a) typical rectangular cantilever and (b) tip of the cantilever [2, 3].

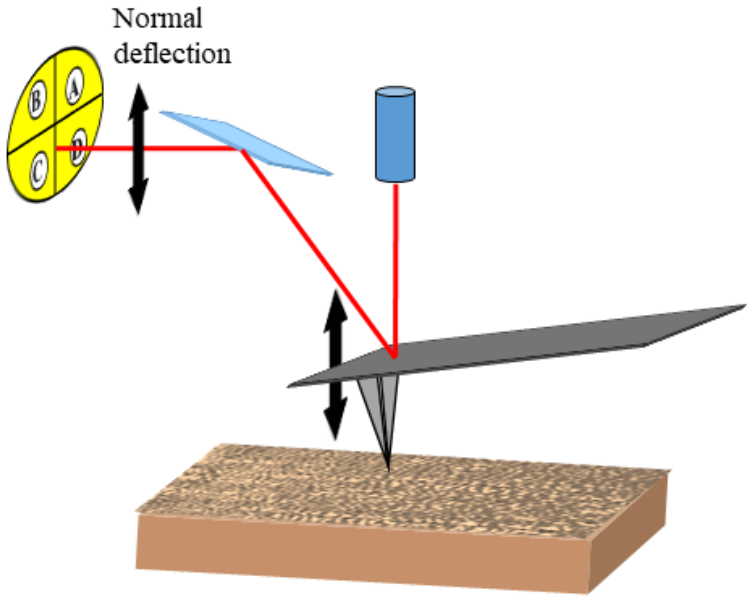

(a)

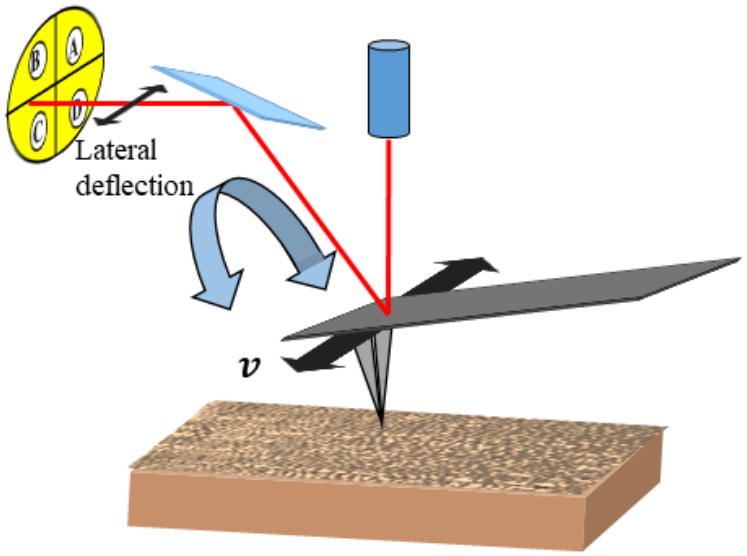

(b)

Figure 3.3: Schematic representation of normal (a) and lateral (b) deflection for cantilever.

3.2 Measurement Preparation

Prior to performing any measurement, the AFM must first be set up. Next the instrument needs to be calibrated for both normal and lateral forces. After that, before to taking any measurement, the samples need to be prepared (cut and clean), and finally measurements are performed on the samples.

3.2.1 Instrument Setup

As shown in Figures 3.4 and 3.5 the systm consists of the following list:

- Digital instrument Multimode AFM: The AFM microscope used in this work was a Digital Instrument Multimode AFM which can perform both non-contact (tapping) and contact (imaging) modes.
- Controller and Extender: Both the controller and extender are responsible to exchange information between the computer and the AFM. This information consists of applying the gain voltages as well as converting the photo currents to voltages.
- Computer: The computer provides the software platform to control AFM and save all acquired data.
- Control and Display monitors: The control monitor is connected to the computer, which is used to display the AFM images while the display monitor is used to observe the image of the surface.
- Camera and light: These tools are used to observe the surface and cantilever

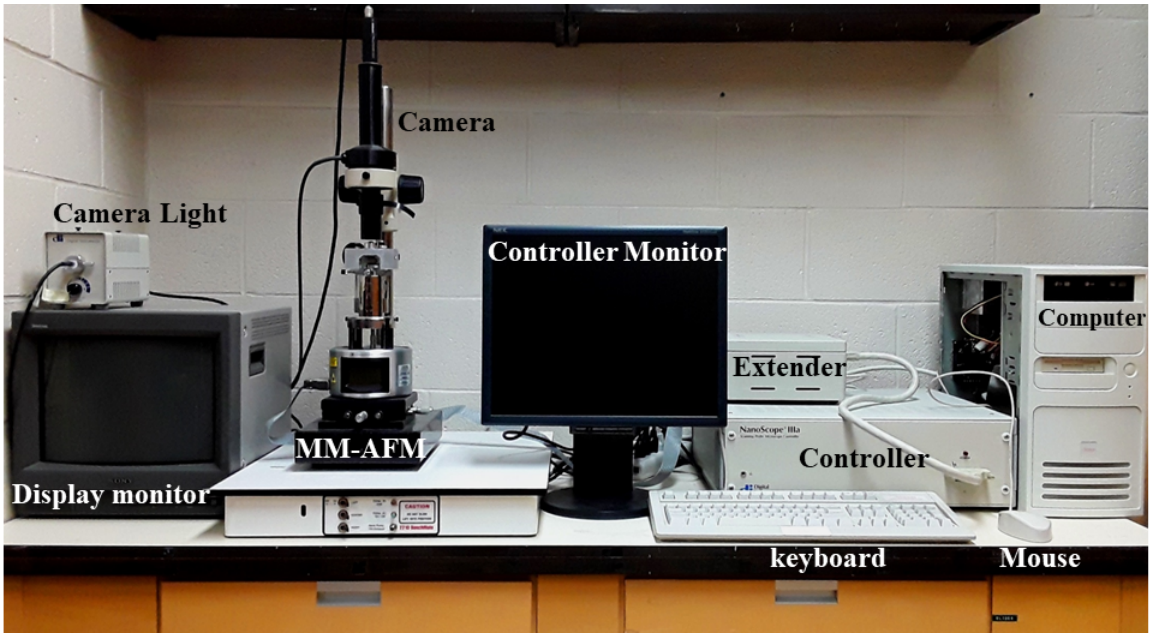

Figure 3.4: Measurement Instruments

3.2.2 Sample and Cantilever Loading

After setting up the instruments, the cantilever and sample need to be installed in the AFM. The sample should be cut such as not to touch the inside wall of the AFM head. The maximized diameter and height of the sample are 15 mm and 8 mm respectively. It is essential to install the sample prior to mounting the probe. Otherwise, when the sample is loaded, the cantilever could get damaged. After the sample is installed, the cantilever is carefully mounted on the probe holder. If the cantilever is installed correctly, the edge of the cantilever and side edge of the cantilever holder stand should be parallel. Now, the cantilever holder is ready to be installed on the AFM head. The above is summarized in Figure 3.7 and 3.6.

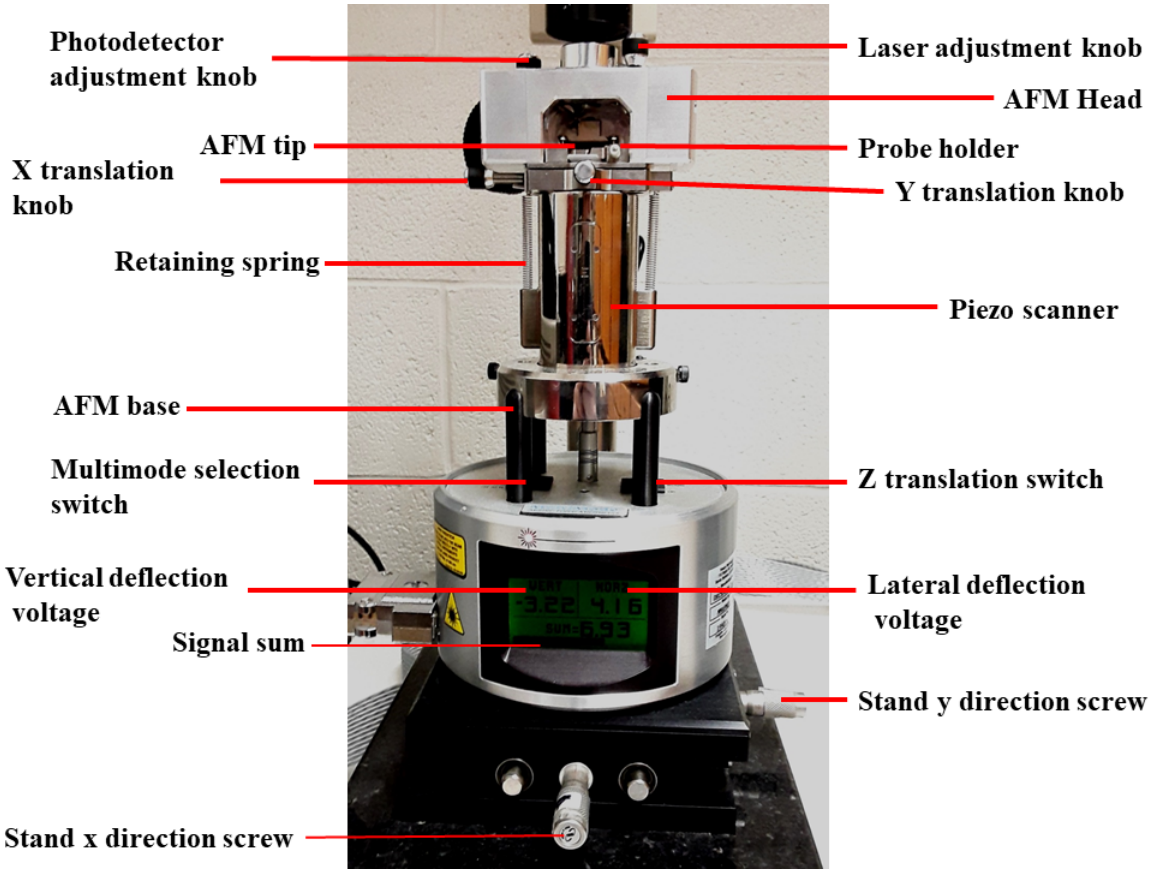

Figure 3.5: Multimode AFM

3.2.3 Laser Alignment

Another step before performing an experiment is aligning the laser on the free end of the cantilever. Two approaches are taken to align the laser on the cantilever. In the first case, using the optical camera and the monitor, the laser beam is located on the cantilever as best as possible. After that, using the x and y knobs for adjusting the laser position, the laser beam is brought on top of the cantilever so that the sum signal bar reaches a maximum. When the laser is aligned properly the intensity value should be between 6.90 volt and 7.20 volt for a gold coated silicon cantilever.

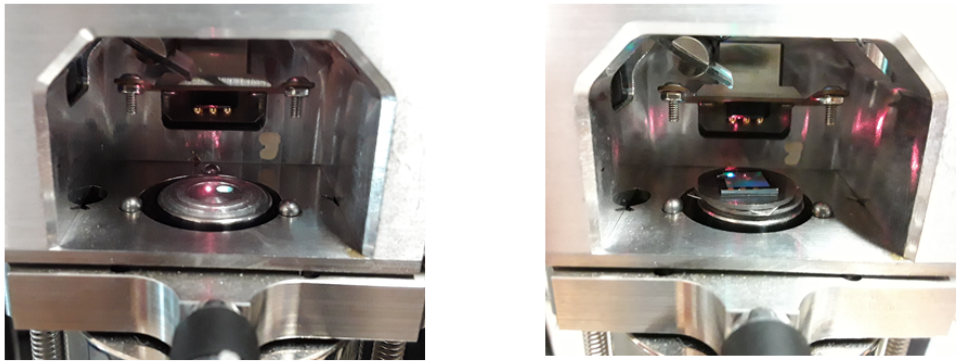

Figure 3.6: Scanner with (right) and without (left) sample [4]

3.3 Calibration

After the instrument has been properly initiated, the machine is ready to be used to perform measurements. Since, the measured data is required to be converted properly from units of volts to units of force in Newtons, the normal and lateral calibration factors need to be calculated. Therefore the next step in experiment is to determine the calibration factors.

3.3.1 Normal Load Calibration

To calculate the normal load it is necessary to produce force versus distance curve. The force-distance curve gives information about the deflection of the cantilever and the force between the tip and sample, which is related to the distance of the cantilever from the surface. A cantilever can be modeled as a spring of stiffness k fixed at one end with the tip at the other end. The applied force on the tip, deflects the cantilever which changes its distance from the surface according to the Hook's law ($F = -kz$

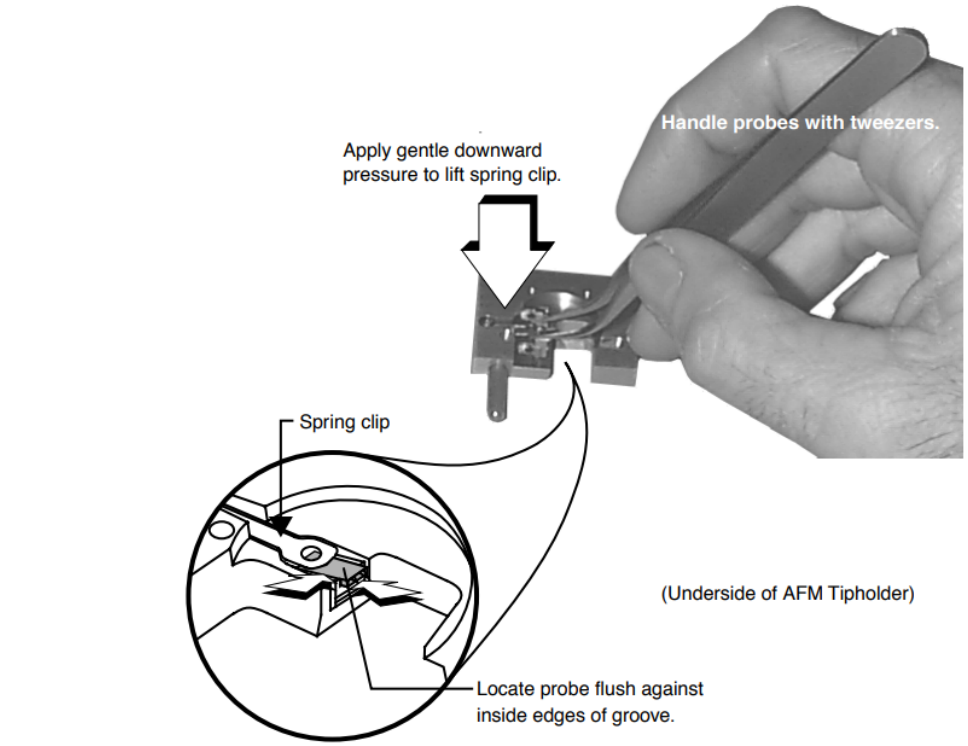

(a)

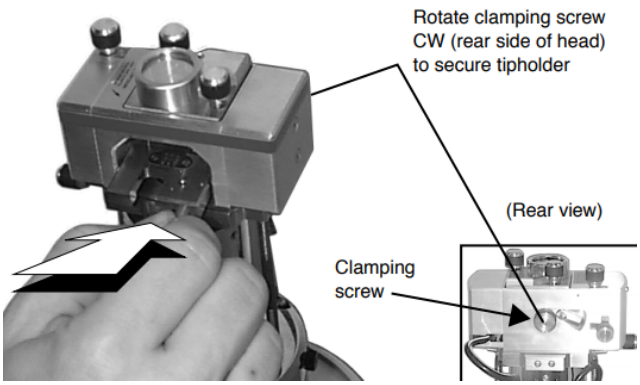

(b)

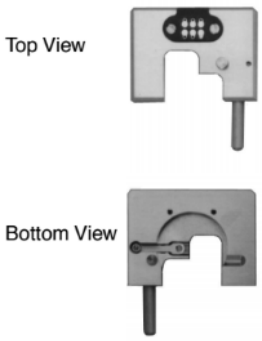

(c)

Figure 3.7: (a) Inserting cantilever under the spring clip, (b) Installing the probe holder inside the AFM head, (c) Probe holder [4]

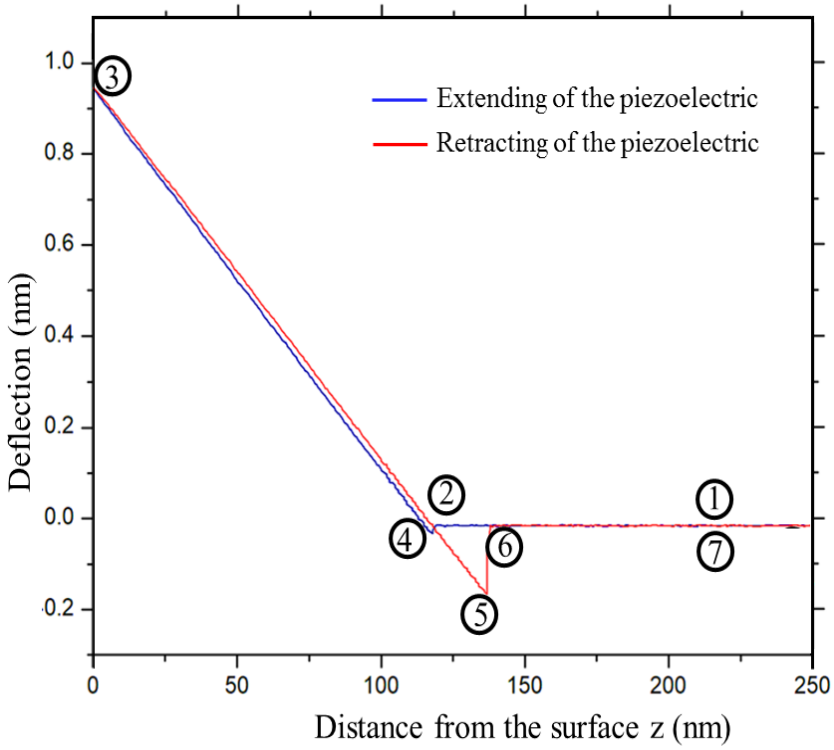

Figure 3.8: The plot shows how the force is exerted onto the surface, which is collected from the force calibration plot over the sample surface.

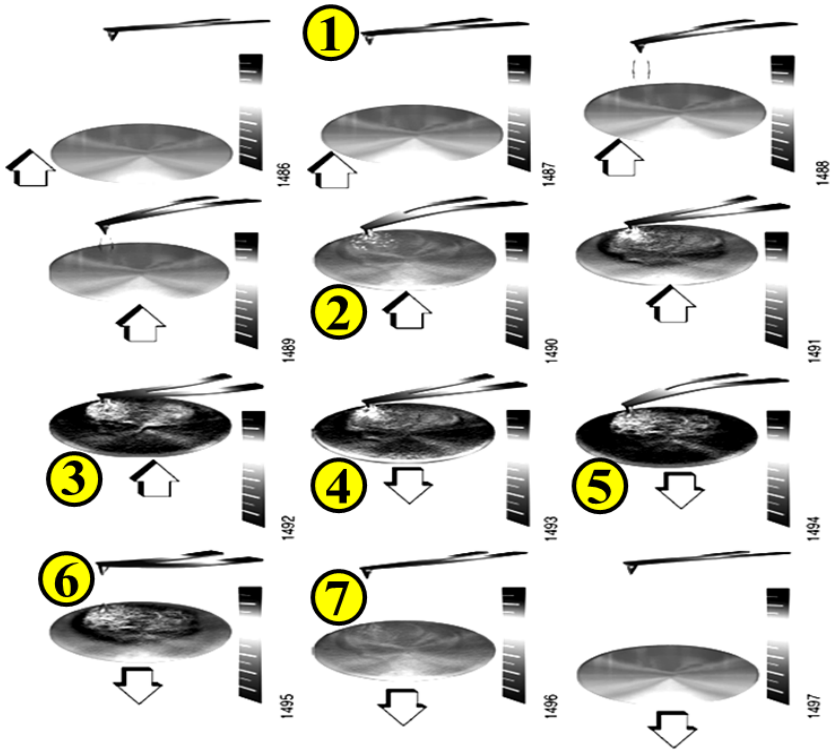

Figure 3.9: Tip-sample interaction during the extending and retraction of the piezoelectric tube. [5]

where z is the change in length from its equilibrium position).

Figure 3.8(a) shows the interaction force between the cantilever tip and the surface of the sample as function of height. At point 1, the cantilever is above the surface. Between point 1 and 2 the sample is raised towards the tip. At point 2, the tip is pulled down and makes contact with the sample, and continues pressing the tip onto the surface causing the cantilever to bend upward until point 3. From point 3 to point 4, the tip still remains in contact with the surface; From point 4 to point 5, the tip remains in contact with the surface causing the cantilever to bend downward, due to the adhesion force between tip and surface. After further retraction of the sample, the tip finally detaches at point 5. From point 6 the cantilever remains undeflected till point 7. From the force-distance curve shown in Figure 3.8, the deflection of the cantilever in the z-direction can be determined. The slope of the curve from the inclined part of the graph (between point 3 and 5) is known as sensitivity which is defined as:

$$U_v = S_v z. \tag{3.1}$$

The sensitivity is calculated by the Nanospcope automatically when the sloped part of the force curve is selected. The system converts z deflection displacement in units of volt to units of length (nm). The deflection is the amount that the cantilever bends from its equilibrium position at the free end calculated from Equation 3.2 where set point (V_{csmin}) is the value of force distance curve at point 5 in Figure 3.8. By having the deflection displacement and stiffness of the cantilever, the normal load can be calculated in units of nano Newton (nN) from the Hook's law. Equation 3.2 is used

to determine the tip distance from the surface in nanometer (nm).

$$z = (V_{csmin}(\text{Volt})) \times (S_v^{-1}(\text{nm/Volt})) \tag{3.2}$$

The cantilever stiffness can be calculated using theoretical or experimental methods [28–32]. We used the theoretical method base on the geometry of the cantilever and an experimental method based on the natural resonance frequency (NRF) of the cantilever. In the geometric method the cantilever stiffness is calculated from physical properties of the cantilever, such as length L, width w, thickness t as well as the cantilever's Young's modulus E [30,33]. Equation 3.3 shows the relationship between the cantilever normal stiffness and geometrical properties of a rectangular cantilever:

$$k_z = \frac{Et^3w}{4L^3}. \tag{3.3}$$

Here, Young's modulus E depends on cantilever material, which for our experiments was silicon.

Another method which we used to determine the cantilever stiffness is the NRF method, which was introduced by Cleveland *et al.* [31]. In this approach, the stiffness is defined as:

$$k_z = 2\pi L^3 w \sqrt{\frac{\rho^3}{E}} (\omega_0)^3, \tag{3.4}$$

where ρ is the cantilever density, E is Young's modulus, and ω_0 is the unloaded resonance frequency of the cantilever. The resonance frequency is the frequency related to the peak of amplitude versus the drive frequency curve (see Figure 3.10).

The normal load was calculated according to Equation 3.5:

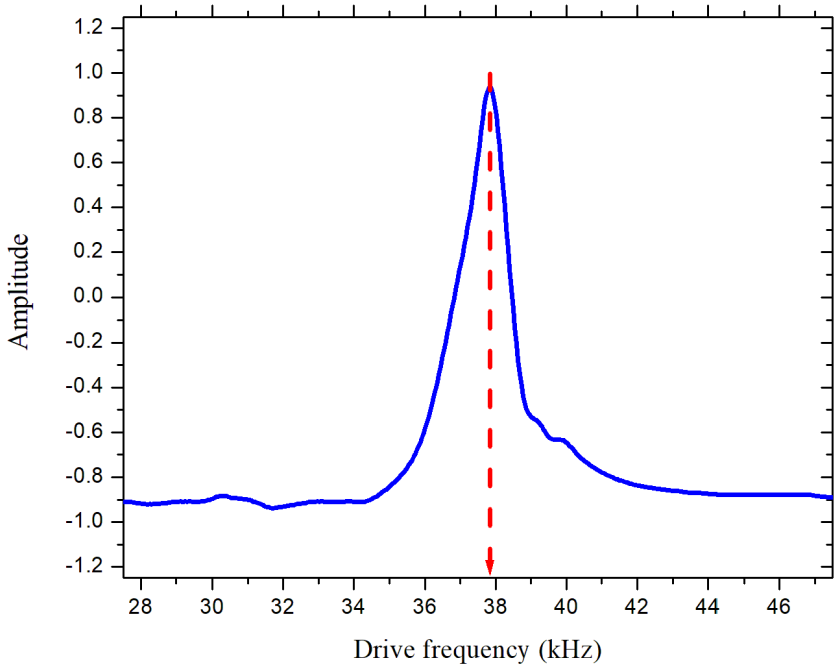

Figure 3.10: Amplitude versus drive frequency

$$\begin{aligned} F_n &= k_z z \\ &\approx \frac{Et^3 w}{4L^3} \times \frac{V_{csmin}}{S_v} \\ &\approx 2\pi L^3 w (\omega_0)^3 \sqrt{\frac{\rho^3}{E}} \times \frac{V_{csmin}}{S_v}. \end{aligned} \tag{3.5}$$

It should be noted that, the cantilever stiffness calculated from the geometric and the resonance frequency methods are not necessarily equal. A comparison of both geometrical and NRF approaches for a typical silicon cantilever is given in Table 3.2. Because the geometric approach has more substantial uncertainty and also as the NRF method performed in ambient conditions, the result of the NRF method would be close to the value when water vapor exists. In this work, the cantilever stiffness

was calculated using the NRF method. Physical properties of the conventionally used cantilever are listed in Table 3.1.

Physical quantity	value
Thickness (t)	2.4 ± 0.1 μm
Width (w)	51 ± 1 μm
Length (L)	450 ± 1 μm
Resonance frequency (ω_0)	37.83 ± 0.01 kHz
Density (ρ)	2330 ± 1 kg/m^3
Young's Modulus (E)	165 ± 1 GPa

Table 3.1: Silicon cantilever's physical properties (k_z)

geometrical approach	0.32 ± 0.04 (N/m)
natural resonance frequency method	0.438 ± 0.004 (N/m)

Table 3.2: Calculated and measured vertical spring constant (k_z)

3.3.2 Lateral Force Calibration Theory

As for the normal load calibration, there are different methods to performe the lateral force calibration. The lateral force calibration is used to convert the lateral deflection

in units of volts to values of force in units of Newton. The *wedge* method is one calibration methods which applies a specific sample ($SrTiO_3$) with known surface topography to calculate the conversion factor for lateral forces [34]. Recently, Michelle L. Gee *et al.* has modified this method by [35] using the calibration grating (TGF11). In this modified method, the authers argued that adhesion force, which affects the friction value, should be considered, which in the original *wedge* method was not considered. Also for commercial AFMs, the trace and retrace signals are not equal which leads to different values of the friction for the trace and retrace scanning [35–38]. Considering adhesion force and inequality of the trace and retrace signals were the basic modification for their method. In the following, we will discuss all the procedures of the calibration method. Still, before that, it is required to discuss the theory behind the lateral calibration in details by considering the schematic diagram of hypothetical friction data (3.11).

Friction measurements are conducted by trace and retrace scanning of the sample in the direction perpendicular to the length of the cantilever with a constant tip velocity. This motion leads to a twisting of the cantilever in the opposite direction to the scan direction. Torsional deflection is detected as a lateral voltage ($V_{lateral}$) by the PSD, which is related to the lateral force on the cantilever tip (friction force) by the conversion factor α (not to be confused with the inverse characteristic length in the off-rate equation (2.7)):

$$F_{lateral} = \alpha V_{lateral}. \tag{3.6}$$

For each friction loop recorded with different normal loads, two parameters, the

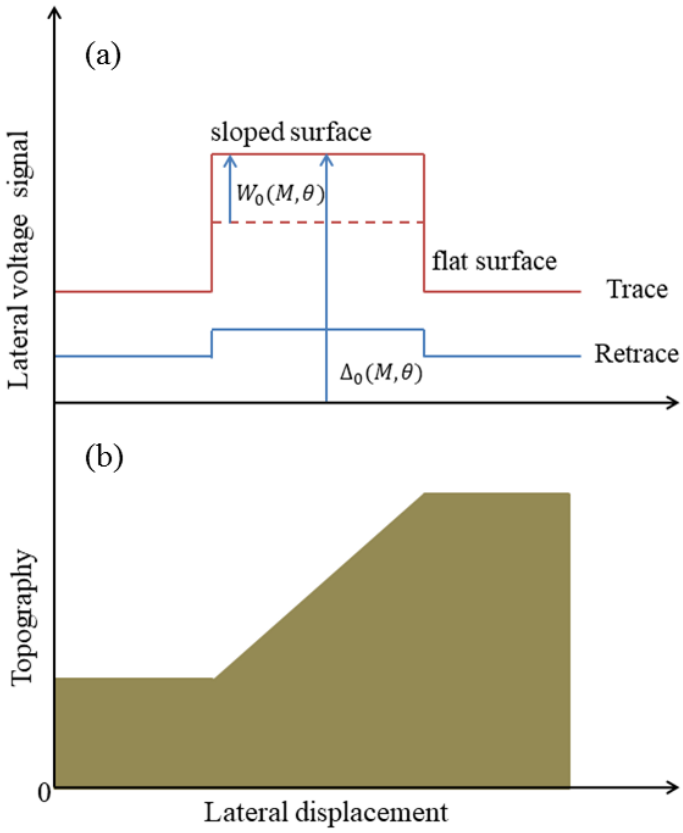

Figure 3.11: (a) Schematic cross section of friction loop. (b) The calibration grating surface on the sloped edge

half width of the friction curve $W_0(M,\theta)$ and the offset of the friction curve $\Delta_0(M,\theta)$ are obtained for each of the trace and retrace parts separately, which both are functions of the edge angle θ and torsional moment M_u and M_d. In Figure 3.11 these parameters are shown for the trace part of the friction loop only [36]. These parameters are in units of volt and should be related to torsional moment using the conversion factor α.

To calculate the conversion factor, α, see Figure 3.12, friction force, f_u, and effective adhesion force, F_A, should be balanced by the constant applied normal load,

f_{load-u} and lateral force, $F_{lateral-u}$ as written in Equations 3.7. Also, the torsional moment should be related to $F_{lateral-u}$ by tip length and the cantilever thickness, h and t according to the Equation 3.8. In addition, relation between the torsional moment and the conversion factor is written in Equation 3.9.

$$\begin{aligned} F_{lateral-u} &= \frac{F_{load-u} sin\ \theta + \mu(F_{load-u} cos\ \theta + F_A)}{cos\ \theta + \mu sin\ \theta} \\ F_{lateral-d} &= \frac{F_{load-d} sin\ \theta - \mu(F_{load-d} cos\ \theta + F_A)}{cos\ \theta - \mu sin\ \theta} \end{aligned} \tag{3.7}$$

$$\begin{aligned} M_u &= F_{lateral-u}(h + t/2) \\ M_d &= F_{lateral-d}(h + t/2) \end{aligned} \tag{3.8}$$

$$\begin{aligned} W_0(M, \theta) &= \frac{M_u - M_d}{\alpha(2h + t)} \\ \Delta_0(M, \theta) &= \frac{M_u + M_d}{\alpha(2h + t)}. \end{aligned} \tag{3.9}$$

It is expected that since the deflection set-point is constant during the scanning, the normal load during the upward motion, f_{load-u}, be equal to the normal load during the downward motion f_{load-d}. However, this assumption is incorrect and f_{load-u} and f_{load-d} are not equal even when the gain voltages are properly adjusted. On the other hand, Johnson *et al.* showed under the constant normal load, breaking of the junctions between the tip and the surface break non-monotonically due to the sliding [39] which means that exerted normal load can change by motion. Based on these two aspects of the normal load Gee *et al.* provided the following Equation 3.10 for $W_0(M, \theta)$ and $\Delta_0(M, \theta)$ as measured quantities in terms of expected values ($W_0^0(M, \theta)$ and $\Delta_0^0(M, \theta)$) with correction terms (W_0^a and Δ_0^a, W_0^b and Δ_0^b, W_0^c and

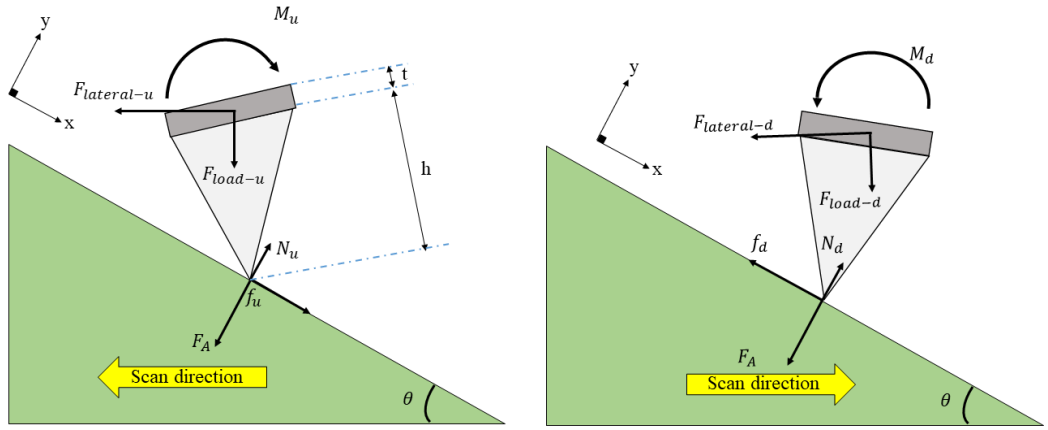

Figure 3.12: Schematic diagram showing a moving cantilever on the surface of the grating. (a) Upward scanning (b) downward scanning.

Δ_0^c). The first error terms W_0^a and Δ_0^a are related to the coupling of the vertical and lateral deflection voltages, the second error terms W_0^b and Δ_0^b are related to poor electrical feedback systems setup and the last error terms W_0^c and Δ_0^c are related to optical interference, which produces noise in the friction loops.

$$\begin{aligned} W_0(M,\theta) &= W_0^0(M,\theta) + W_0^a(M,\theta) + W_0^b(M,\theta) + W_0^c(M,\theta) \\ \Delta_0(M,\theta) &= \Delta_0^0(M,\theta) + \Delta_0^a(M,\theta) + \Delta_0^b(M,\theta) + \Delta_0^c(M,\theta). \end{aligned} \tag{3.10}$$

Equations 3.10 indicate that to calculate the conversion factor, α, it is required to subtract the errors from the measured values of half width $W_0(M,\theta)$ and offset $\Delta_0(M,\theta)$. By replacing the $W_0(M,\theta)$ and $\Delta_0(M,\theta)$ with $W_0^0(M,\theta)$ and $\Delta_0^0(M,\theta)$ in Equations 3.9, 3.7 and 3.8 new equations are written as:

$$\alpha W_0^0(M,\theta) = \frac{\mu}{2}\frac{(F_{load-u} + F_{load-d} + 2F_A\ cos\ \theta)}{cos^2\ \theta - \mu^2 sin^2\ \theta} + \frac{\mu^2+1}{2}\frac{(F_{load-u} - F_{load-d})cos\ \theta sin\ \theta}{cos^2\ \theta - \mu^2 sin^2\ \theta} \tag{3.11}$$

$$\alpha\Delta_0^0(M,\theta) = \frac{1}{2}(\frac{(\mu^2+1)((F_{load-u} + F_{load-d})cos\ \theta sin\ \theta}{cos^2\ \theta - \mu^2 sin^2\ \theta}) + \frac{1}{2}\frac{2\mu^2 F_A\ sin\ \theta\ + \mu((F_{load-u} - F_{load-d})}{cos^2\ \theta - \mu^2 sin^2\ \theta}\ . \tag{3.12}$$

The normal load deviates from the set point value F_{load-u} by the value of ΔF_{load}. The upward and downward scanning normal loads are written in the form of Equations 3.13:

$$F_{load-u} = F_{load} + \Delta F_{load}$$
$$F_{load-d} = F_{load} - \Delta F_{load}. \tag{3.13}$$

Putting the Equations 3.13 into Equations 3.11 and 3.12 yields:

$$\alpha W_0^0(M,\theta) = \frac{\mu F_{load}}{cos^2\ \theta - \mu^2 sin^2\ \theta} + \frac{\mu F_A\ cos\ \theta + (\mu^2+1)\Delta F_{load} cos\ \theta sin\ \theta}{cos^2\ \theta - \mu^2 sin^2\ \theta}. \tag{3.14}$$

$$\alpha\Delta_0^0(M,\theta) = \frac{(\mu^2+1)F_{load} cos\ \theta sin\ \theta}{cos^2\ \theta - \mu^2 sin^2\ \theta} + \frac{\mu^2 F_A\ sin\ \theta\ + \mu\Delta F_{load}}{cos^2\ \theta - \mu^2 sin^2\ \theta}\ . \tag{3.15}$$

Now we can rewrite the above equations in a more simple form as:

$$W_0^0 = S_w F_{load} + I_w$$
$$\Delta_0^0 = S_\Delta F_{load} + I_\Delta, \tag{3.16}$$

where,

$$
\begin{aligned}
S_w &= (\frac{1}{\alpha})\frac{\mu}{cos^2\ \theta - \mu^2 sin^2\ \theta} \\
S_\Delta &= (\frac{1}{\alpha})\frac{(\mu^2+1)cos\ \theta sin\ \theta}{cos^2\ \theta - \mu^2 sin^2\ \theta} \\
I_w &= (\frac{1}{\alpha})\frac{\mu F_A\ cos\ \theta + (\mu^2+1)\Delta F_{load} cos\ \theta sin\ \theta}{cos^2\ \theta - \mu^2 sin^2\ \theta} \\
I_\Delta &= (\frac{1}{\alpha})\frac{\mu^2 F_A\ sin\ \theta\ + \mu\Delta F_{load}}{cos^2\ \theta - \mu^2 sin^2\ \theta}.
\end{aligned}
\tag{3.17}
$$

Equations 3.16 show that the corrected half-width and offset are linear function of average load, and the slope of these linear equations yield the coefficient of friction μ and the conversion factor α respectively. Since, the adhesion force, F_A, and the normal load deviation, ΔF_{load}, do not contribute to S_w and S_Δ, the conversion factor is not related to the adhesion force and the normal load deviation. As a consequence, using the slopes S_w and S_Δ related to the Equation 3.16 plotted with different normal loads gives the friction coefficient μ and the conversion factor α.

3.3.3 Lateral Force Calibration Experiment

For the calibration, all experiments were performed using contact mode rectangular silicon cantilevers with a corresponding nominal thickness of 1 μm, length of 450 μm, and stiffness of 0.2 N/m as purchased from NanoWorld AG (Switzerland). A commercial trapezoidal calibration grating (TGF11) from NanoAndMore USA was used for the calibration. The sidewalls are 54.7° from the horizontal surfaces, which is known as the edge angle, with a steps height of 1.75 $\pm$ 0.01 μm (see Figure 3.13). The calibration sample required to be carefully aligned such that the facets of the samples were parallel to the length of the cantilever. Once the sample was aligned, force curve

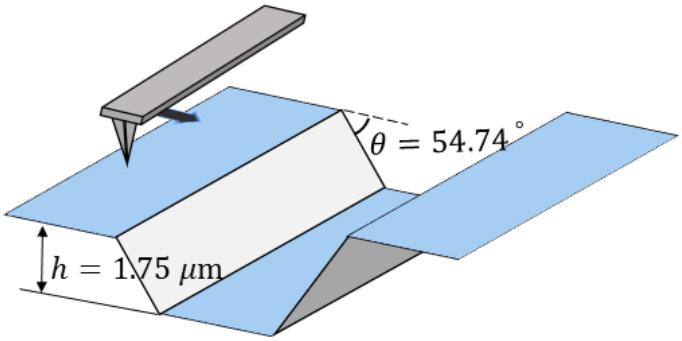

Figure 3.13: Schema of the trapezoidal calibration grating

measurements were conducted on the flat part of the sample to avoid any twisting of the cantilever during the measurement. As discussed in section 3.3.1, the force curve provides the normal load and the vertical distance from the flat surface. Changing the deflection set-point produces different normal loads, which are required to to plot Equations 3.16 and 3.17 in different normal loads. To produced the different normal loads, the deflection set points was changed from -2.5 Volt to 3.0 Volt and plotted as shown in Figure 3.14.

Each normal load would be used to produce a different friction loop. The collected data was related to 50 different normal loads and the tip velocity was set to be 5 μm/s for all measurements. After changing the normal load, the gain voltage was altered such as to produce images that had acceptable quality and clearness. The scanning direction during the data acquisition was perpendicular to the cantilever alignment. All collected image data were exported in ASCII format to use the data in Excel software. An example of the friction data for a given normal load is shown in Figure 3.15:

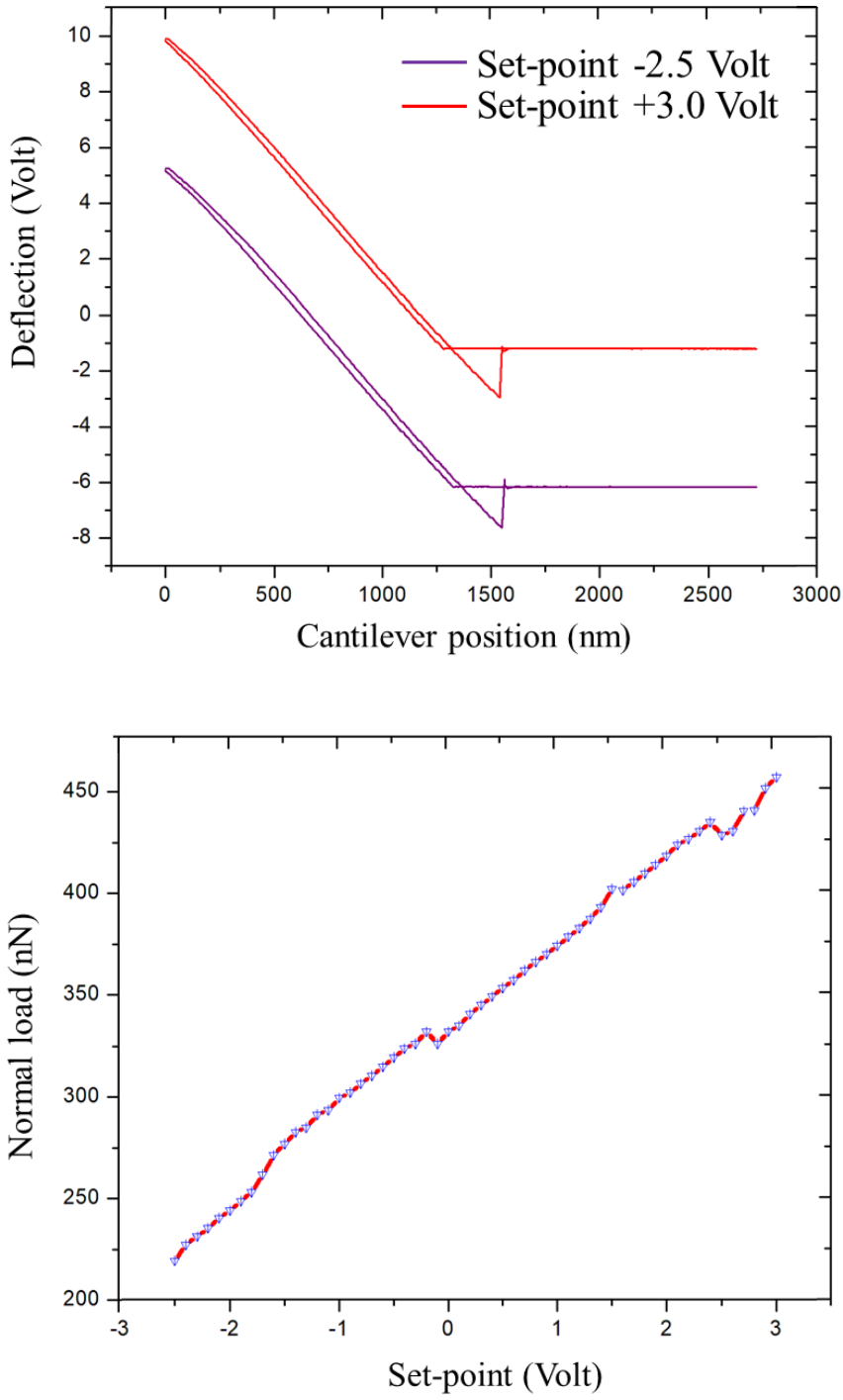

Figure 3.14: (a) Range of the normal load between red (highest normal load) and blue (lowest normal load). (b) Normal vs. the set points calculated from the force curve.

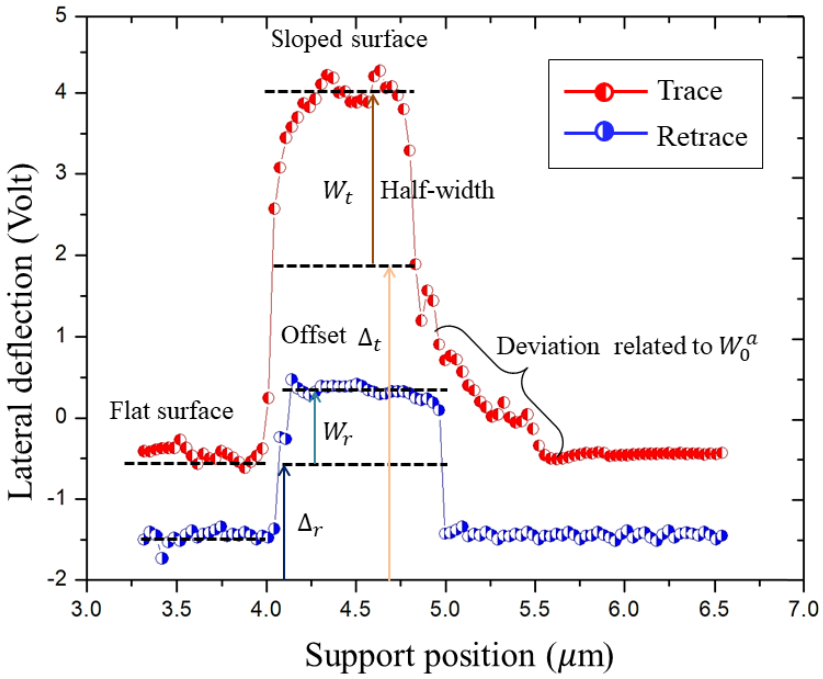

(a)

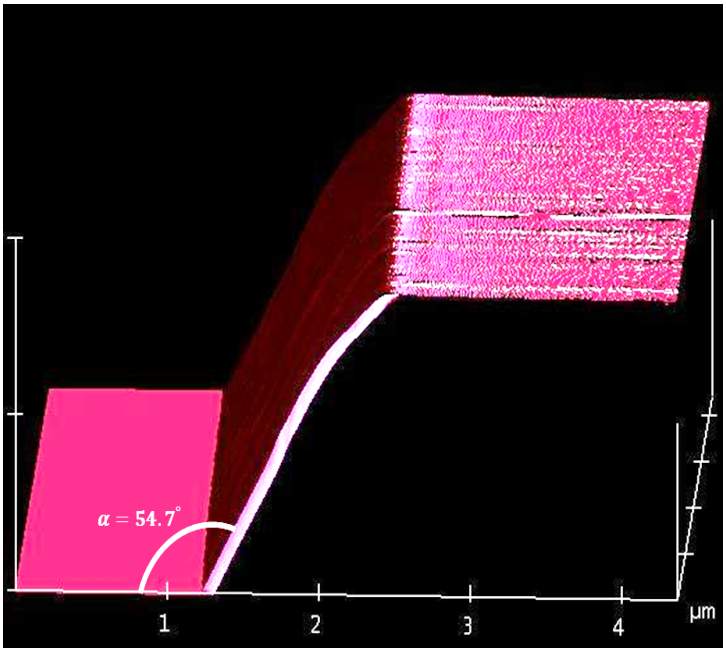

(b)

Figure 3.15: (a) Lateral deflection, half width and offset, (b) Topography of the sloped facet.

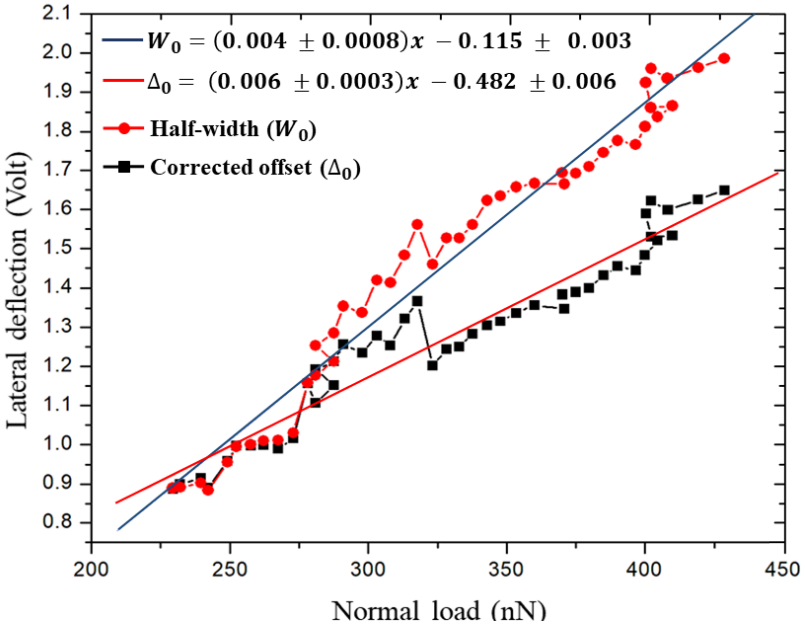

(a)

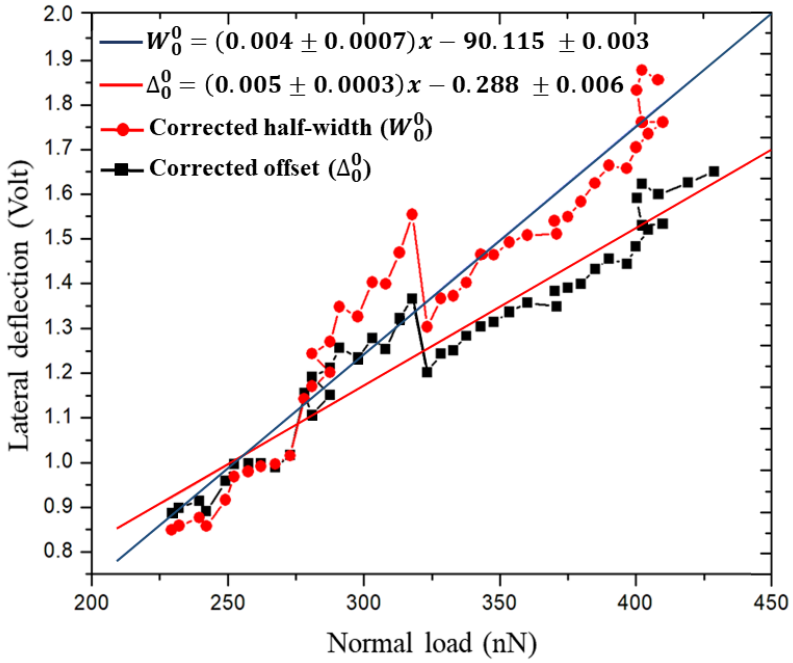

(b)

Figure 3.16: (a) Measured halfwidth $W_0(M, \theta)$ and offset $\Delta_0(M, \theta)$ versus the normal load (b) Corrected halfwidth $W_0^0(M, \theta)$ and offset $\Delta_0^0(M, \theta)$ versus the normal load.

From the friction data, the aim is to find the measured half width, $W_0(M,\theta)$, and offset, $\Delta_0(M,\theta)$, for a given normal load. Figure 3.16(a) represents the the friction loop including the half-width, $W_0(M,\theta)$, the offset, $\Delta_0(M,\theta)$, and deviation error $W_0^0(M,\theta)$. Regardless of how the data were obtained, the data needed to be corrected according to Equations 3.10. If the laser alignment and feedback systems are set up properly, both errors corresponding to the dynamic coupling between vertical and lateral voltage, W_0^b and Δ_0^b, and the optical interference, W_0^c and Δ_0^c, can be neglected. However, errors related to static coupling, W_0^a and Δ_0^a, can not be ignored. These errors can be evaluated from the offset values of the friction data taken from the flat surface of the sample. Since on the flat part of the sample the offset would not deviate from the half-width, any deviation should be considered as error, W_0^a and Δ_0^a. From Figure 3.15(a) the deviations from the half-with on the flat surface is shown in the trace graph of the friction loop. Comparing both Figures 3.16(a) and 3.16(b) illustrates the differences before and after the error subtraction. Fitting the data with a linear equation yields the slope S_W and S_Δ defined in Equations 3.16. Using the S_W and S_Δ leads to calculate the conversion factor (α) and friction coefficient (μ) from Equations 3.17. Calculated values for these two coefficients are reported in Table 3.3.

calculated quantity	value
coefficient friction (μ)	0.36 ± 0.09
Conversion factor (α)	25 ± 3 nN/V

Table 3.3: Calibration results

3.4 Sample Cleaning

Before conducting out experiment, our samples needed to be thoroughly cleaned. Any sample exposed to the atmosphere will be covered by airborne contaminants which would not provide accurate measurements of friction between the sample and the Si tip.

In this work two types of substrates were used, regular glass, and mica. To obtain a clean surface of mica is simple. Mica has a layer structure allowing it to be cleaved easily. The top layer of the mica surface can be exposed by applying an adhesive tape and then pulling it off. The adhesive will peel away one or sometimes several mica layers exposing a pristine surface free of any contaminants.

The cleaning procedure of glass is more complicated because the contaminants on glass have usually accumulated for a long time and vary in the type of contaminant. For this purpose, there are several methods used to clean glass [40–42]. In general, there are three main wet-based procedures for cleaning the glass, which is accomplished by using different types of acidic solutions, alkaline solutions, and organic solutions. The method used in this work for cleaning glass is the same approach described by Ligler *et al.* [41]. Before staring the cleaning process, all containers were washed using detergents and rinsed carefully using de-ionized water (DW) to make sure all detergent residues were removed. The steps for cleaning glass are as follow:

1) The samples were suspended for 30 minutes in a mixture of 100 mL of hydrochloric acid (HCl) and 100 mL methanol (MeOH). After 30 minutes the samples were

rinsed with DW. 2) The samples were placed in concentrated sulfuric acid (H_2SO_4) for 30 minutes at 60° C. After 30 minutes, samples were rinsed with DW. 3) Because sulfuric acid was concentrated, the samples were boiled in DW for 30 minuts. 4) After this, the samples were placed for 5 to 10 minutes in a mixture of ammonium oxide (NH_4OH), hydrogen peroxide ((30%)H_2O_2), and water (H_2O) with a ratio of 1:1:5 at a temperature of 80° C. 5) After rinsing the samples with DW, the samples were placed in a mixture of hydrochloric acid (HCl), hydrogen peroxide ((30%) H_2O_2), and water (H_2O) with ratio of 1:1:5 for 5 to 10 minutes at 80° C. 6) After rinsing the samples with DW, they were placed in a solution of 10% potassium hydroxide (KOH) desolved in isopropyl alcohol (isopropanol) for 30 minutes. 7) For the next step, samples rinsed with DW and placed in a one molar solution of sodium hydroxide (NaOH) for 20 minutes. 8) The last part of the sample washing process was to clean the samples in a piranha solution which is the mixture of sulfuric acid (H_2SO_4) and hydrogen peroxide ((30%) H_2O_2) in a ratio of (3:1) at 80° C for 20 min. Finally, the samples were rinsed thoroughly with DW and dried by blowing nitrogen gas to remove liquid from the sample surface and become dry. Steps one, five and six were used to clean inorganic materials, while steps two, four, seven, and eight were used to clean organic materials. After this cleaning process, the samples were ready for processing.

3.5 Measurements on Glass and Mica

Samples 1 cm×1 cm in size were mounted to the sample holder, using two-sided adhesive tape and then mounted in the AFM sample mount. After mounting the

chip holder in the AFM head, the alignment of the laser on the cantilever was done. A properly aligned laser beam on the cantilever was indicated by a maximum signal bar, as seen by the signal display in Figure 3.5. In the next step, the vertical and horizontal voltages were set. The minimum value of the vertical voltage should be set between -5 V to -3 V in order to have reproducible topography images with minimum noise. The horizontal voltage, which corresponds to the lateral force and torsional bending of the cantilever, was set to zero. The sample was scanned in a direction, perpendicular to the length of the cantilever. Different scanning velocities were used from 0.5 μm/s to 2 μm/s in steps of 0.1 μm/s. It should be noted that for each chosen velocity, the gain voltages (integral and proportional) had to be carefully adjusted until both the trace and retrace value of the topography were as close to each other as possible. For a given normal load, the pulling velocity was changed from 0.5 μm/s to 2 μm/s. The procedure was done for different normal loads in the range of -2 V to +3 V. It is important to note that all measurements should be performed over the same area of the sample. The Nanoscope was set to a scan an area of 32 lines and save in one image. The analysis of the saved data is the objective of Section 3.6.

3.6 Experiment Results

A typical friction loop recorded on glass is shown in Figure 3.17. From the topography (blue data) with the ordinate on the right-hand side, it is clear that the surface is flat. The data show that there is no significant change in the surface over the length of 2μm. From the friction loop (red and black curves), it is seen that the friction curve is smooth, with small fluctuations around the average friction. From this measurement,

not only was stick-slip behavior not observed, but also there was no difference between static and kinetic friction. The static friction force is the force required to initiate movement while the kinetic friction is the force that keeps the motion steady and exists while there is motion.

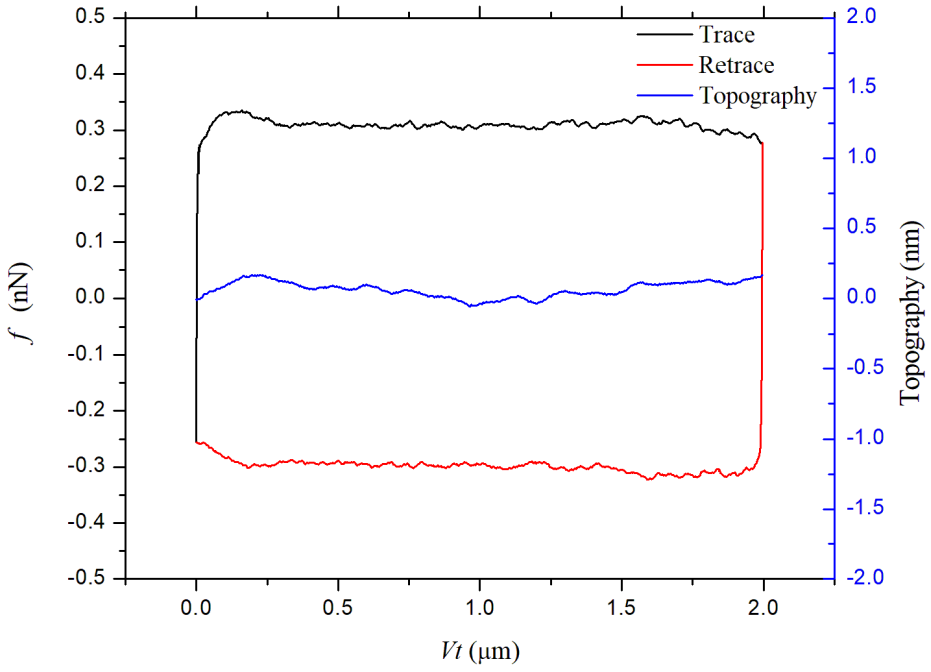

Figure 3.17: Friction loop over the surface of the cleaned glass. The blue curve shows the topography of the surface of glass and the black and red curves show the friction loop. For this particular measurement the pulling velocity is 0.8 μm/s

For a given normal load and pulling velocity, average friction can be obtained from friction loops and plotted against the pulling velocity. Average friction is calculated by considering both trace and retrace parts of the friction loop, excluding the static

friction for both trace and retrace parts of the loops. First we calculate an average value for both trace and retrace parts of a specific interval to exclude the static friction. Then, corresponding absolute values of the trace and retrace are added up and divided by two. This value is the average friction.

The friction data for glass suggests that increasing the pulling velocity causes the average friction to decrease (see Figure 3.19(a)). On the other hand, increasing the normal load, causes the magnitude of the friction to increase for a given pulling velocity.

The results for mica are shown in Figure 3.19(b). At lower normal loads, the average friction is observed to increase with the pulling velocity (the blue and red curve), while at higher normal loads it is decreasing (the black curve). Similar to the results for glass, increasing the normal load causes an increase to the average friction where the lowest normal load shown by the green curve and the highest normal load is shown in black.

3.7 Comparison between simulations and experiment

One conclusion that can be made from a comparison between the stiff-cantilever approximate formula and numerical results for the average friction (see Section 2) is that the stiff-cantilever approximation is very accurate in the steady-sliding regime. Since the stick-slip behaviour was never observed experimentally, we will use our stiff-cantilever approximate formula (2.31), i.e. we set $\kappa_C = \infty$.

Our model contains eight fit parameters: the maximal number of bridges, N_B, the stiffness of a single bridge, κ_B, the damping coefficient of a water bridge, η_B and of the surface, η_S, the bridge formation rate at zero velocity, Ω_{on}, the bridge rupture rate at zero extension Ω_{off}, the characteristic velocity in the formation rate equation, V_0, and the characteristic length in the rupture rate equation, α^{-1}.

It may be argued that with this many parameters, fitting any friction experimental data is trivial. But it turned out that to fit the friction data obtained on glass, it was sufficient to have all parameters fixed except for the maximal number of bridges, N_B and the characteristic velocity V_0. We assumed that the maximum number of bridges is proportional to the normal load. This assumption relies on the reason that by increasing the normal load, the geometry of the contact area changes in a way that allows for more bridges to be formed. Considering these two assumption, fit parameters were produced in terms of try and error process and it was tried to produce a group of data which was close quantitatively to the experimental graph.

However, for mica, in addition to the maximal number of bridges, we had to also assume that at higher normal loads the characteristic velocity V_0 could increase. The reason for this assumption relies on the fact that increasing the characteristic velocity would decrease the formation rate (ω_{on}) which can lead to a declining function of average friction versus pulling velocity at higher normal loads.

The fit parameters related to both mica and glass data are given in Tables 3.4 and 3.5. As can be seen from the tables, N_B increases with the normal load almost linearly (see Figure 3.18). The slopes of N_B versus normal load for mica and glass are 0.79 ± 0.14 and 3.36 ± 0.33 according the linear fit.

The model is in good quantitative agreement with experimental data. With the

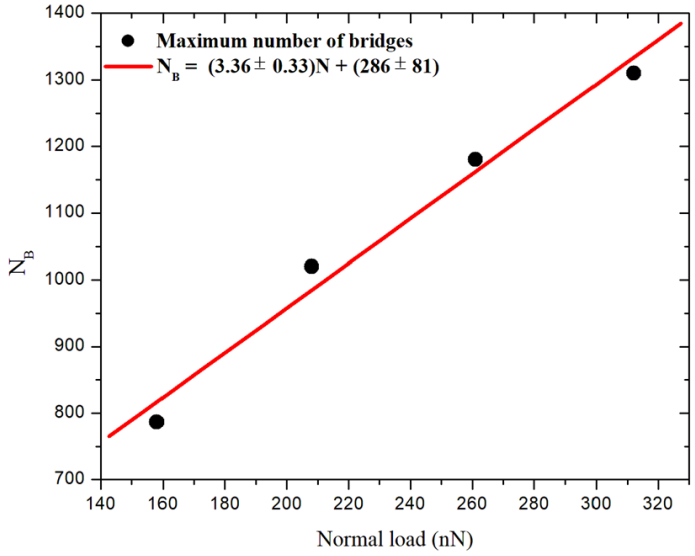

(a)

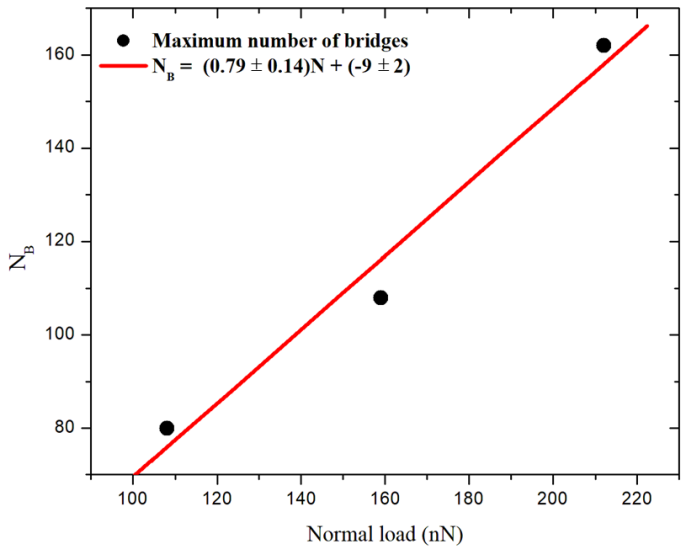

(b)

Figure 3.18: Maximal number of bridges versus the normal load (a) for glass and (b) mica. The red lines represent the linear fits for N_B versus normal load.

Surface	κ_C (N/m)	κ_B (N/m)	η_B ($\frac{\text{nN}}{\text{nm/ms}}$)	η_S ($\frac{\text{nN}}{\text{nm/ms}}$)	Ω_{on} (ms^{-1})	Ω_{off} (ms^{-1})	α^{-1} (nm)
Mica	∞	0.01	0.01	0.01	0.1	0.1	1.75
Glass	∞	0.01	0.009	0.02	0.1	0.1	8

Table 3.4: The fixed fit parameters for the measurements on mica and glass surfaces.

Mica	F_N (nN)	108	159	212	–
	[N_B,V_0 ($\frac{nm}{ms}$)]	[80 , 2]	[108 , 2]	[162 , 14]	–
Glass	F_N (nN)	158	208	261	312
	[N_B,V_0 ($\frac{nm}{ms}$)]	[787 , 2.1]	[1020 , 2.1]	[1180 , 2.1]	[1310 , 2.1]

Table 3.5: Fit parameters for the measurements on glass and mica.

fit parameters from Tables 3.4 and 3.5, the model can reproduce the friction versus pulling velocity curves, see solid lines in Figure 3.19, that are in quantitative agreement with the the experimental data. A comparison between the two different groups of fitting parameters related to glass and mica shows that for glass, the maximal number of bridges, N_B, is higher than for mica. On the other hand, the characteristic length α^{-1} in the rupture rate expression is bigger for glass than for mica. From Table 3.5 it can be seen that characteristic velocity V_0 for glass is always kept fixed while in mica at the higher normal loads its value is larger than the lower normal loads. According to the fitting parameters, damping coefficient η_S and characteristic length α^{-1} related to the glass are larger than for mica.

It cannot be excluded that other combinations of the fit parameters may work

just as good an agreement between the theory and experiment. Clearly, additional measurements are needed to establish the value of those parameters more precisely. This research is left for future work.

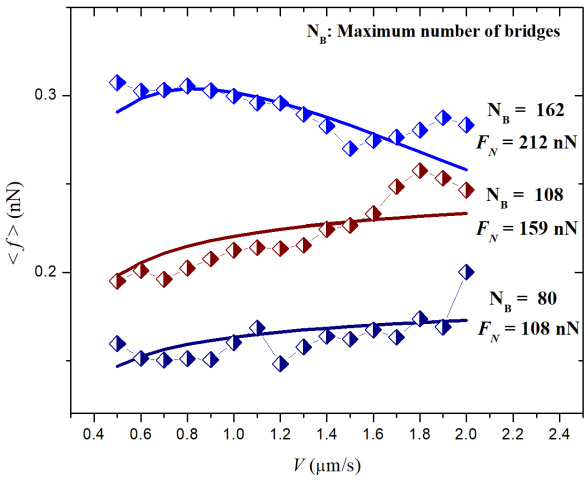

(a)

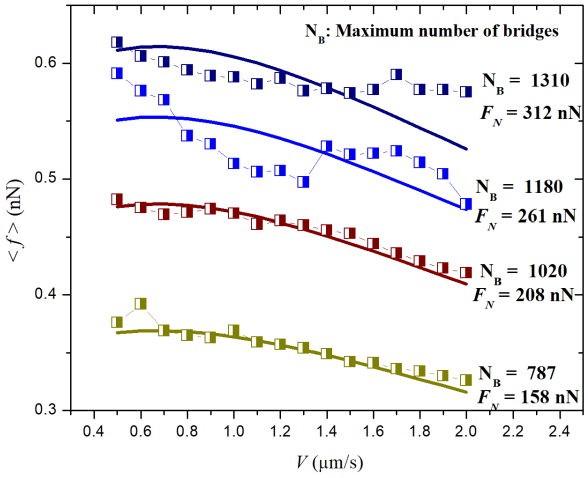

(b)

Figure 3.19: Experimental (symbols) and theoretical (solid curves) average friction force as a function of the pulling velocity for (a) mica and (b) glass substrates at different normal loads. To each normal load value corresponds the maximal number of bridges, N_B

Chapter 4

Conclusion

In this work, we performed the atomic force microscopy to measure the friction on the glass and mica samples in the ambient conditions and simulated the experimental results using the modified mechano-kinetic model. Our experimental results confirm the earlier finding [17, 18] that AFM friction in ambient conditions is mainly due to the formation and rupture of the water bridges between the AFM tip and the surface. In addition, our results indicate that the material of the surface does not have a dominant effect on friction measurement. In ambient conditions, water vapor condensates on top of the surface and can interact with AFM tip by water bridges. Experimental results also show that not only there is no significant difference between static and kinetic friction, but also friction versus position curve fluctuates around the mean friction force. Experimental results indicate that in ambient conditions, AFM friction can increase or decrease with pulling velocity. For the glass surface, it is always decreasing function of pulling velocity, while on the mica, in lower normal loads, average friction increases by pulling velocity. For higher normal loads, it is

declining. Experimental data show that the value of the average friction for both mica and glass is in the same range (0.1 nN to 0.7 nN), and increasing the normal load increases the level of average friction for both mica and glass.

Our modified mechano-kinetic model is capable of reproducing all these features quantitatively. By simulation, we reproduced the same friction curve as the experimental graphs. Our model is modified from the original mechano-kinetic model, and the main difference of our model from the original formulation is that water bridge tails can move along the surface. This modification could be considered as the essential reason for the elimination of the stick-slip behavior from the friction curve, which is more pronounced in the original MK model. The model also can be solved analytically in the limit of the stiff cantilever, which κ_C is much larger than the water bridge stiffness. In this limit, the formation and rupture of the bridges has a little effect on the cantilever tip velocity. Surprisingly, in this limit, our model predicts that the Coulomb friction behaviors is possible if the bond rupture rate is constant. It predicts that when the bond rupture rate is constant, the nanoscale friction is velocity-independent, which is one of the Coulomb friction's features.

The comparison between the original and the modified MK model concludes that depending on the pulling velocity of V, two friction regimes are realized. At low pulling velocity, tip motion proceeds as a steady sliding, whereas at high pulling velocity, the tip exhibits stick-slip behavior. The comparison of the analytical results related to the stiff-cantilever approximation and the numerical results show that in velocities lower than about 5μm/s, the analytical approximation is in perfect agreement with simulation. Higher than 5μm/s, the stiff-cantilever approximation loses its validity.

Bibliography

[1] David J Whitehouse and JF Archard. The properties of random surfaces of significance in their contact. *Proceedings of the Royal Society of London. A. Mathematical and Physical Sciences*, 316(1524):97–121, 1970.

[2] Bert Voigtländer. *Scanning probe microscopy*. Springer, 2015.

[3] Holger Schönherr and G Julius Vancso. *Scanning force microscopy of polymers*. Springer, 2010.

[4] David Ramsdell Karen Gaskell. *AFM Standard Operating Procedure*. Surface Analysis Centre, 2013.

[5] C. Kowalski. *MultiMode SPM Instruction Manual*. Veeco Instruments Inc, 2004.

[6] YT Pei, P Huizenga, D Galvan, and J Th M De Hosson. Breakdown of the coulomb friction law in ti c/ a-c: H nanocomposite coatings. *Journal of applied physics*, 100(11):114309, 2006.

[7] Andrea Vanossi, Nicola Manini, Michael Urbakh, Stefano Zapperi, and Erio Tosatti. Colloquium: Modeling friction: From nanoscale to mesoscale. *Reviews of Modern Physics*, 85(2):529, 2013.

[8] Gerd Binnig, Calvin F Quate, and Ch Gerber. Atomic force microscope. *Physical review letters*, 56(9):930, 1986.

[9] Frank Philip Bowden, Frank Philip Bowden, and David Tabor. *The friction and lubrication of solids*, volume 1. Oxford university press, 2001.

[10] C.M. Mate, G.M. McClelland, R. Erlandsson, and S. Chiang. Atomic-scale friction of a tungsten tip on a graphite surface. *Physical Review Letters*, 59:1942, 1987.

[11] C Mathew Mate, Gary M McClelland, Ragnar Erlandsson, and Shirley Chiang. Atomic-scale friction of a tungsten tip on a graphite surface. In *Scanning Tunneling Microscopy*, pages 226–229. Springer, 1987.

[12] E Gnecco, R Bennewitz, T Gyalog, Ch Loppacher, M Bammerlin, E Meyer, and H-J Güntherodt. Velocity dependence of atomic friction. *Physical Review Letters*, 84(6):1172, 2000.

[13] L Prandtl. A conceptual model to the kinetic theory of solid bodies. *Z. Angew. Math. Mech*, 8:85–106, 1928.

[14] Y. Sang, M. Dubé, and M. Grant. Thermal effects in atomic friction. *Physical Review Letters*, 87:174301, 2001.

[15] A. Schirmeisen, J. Jansen, and H. Fuchs. Tip-jump statistics of stick-slip friction. *Physical Review B*, 71:245403, 2005.

[16] M. Evstigneev, A. Schirmeisen, L. Jansen, H. Fuchs, and P Reimann. Force dependence of transition rates in atomic friction. *Physical Review Letters*, 97:240601, 2006.

[17] E. Riedo, F. Levy, and H. Brune. Kinetics of capillary condensation in nanoscopic sliding friction. *Physical Review Letters*, 88:185505, 2002.

[18] E. Riedo, I. Palaci, and H. Brune. The 2/3 power law dependence of capillary force on normal load in nanoscopic friction. *Journal of Chemical Physics B*, 108:5324–5328, 2004.

[19] A.E. Filippov, J. Klafter, and M. Urbakh. Friction through dynamical formation and rupture of molecular bonds. *Physical Review Letters*, 92:135503, 2004.

[20] I. Barel, A.E. Filippov, and M. Urbakh. Formation and rupture of capillary bridges in atomic scale friction. *Journal of Chemical Physics*, 137:164706, 2012.

[21] R. Capozza, I. Barel, and M. Urbakh. Probing and tuning frictional aging at the nanoscale. *Science Reports*, 3:1896, 2013.

[22] G.I. Bell. Models for the specific adhesion of cells to cells. *Science*, 200:618—-627, 1978.

[23] J. Freund, J. Halbritter, and J.K.H. Hörber. How dry are dried samples? water adsorption measured by stm. *Microscopy Research and Technique*, 44:327—-338, 1999.

[24] G. Zhao, Q. Tan, L. Xiang, D. Cai, H. Zeng, H. Yi, Zh. Ni, and Y. Chen. Structure and properties of water film adsorbed on mica surfaces. *Journal of Chemical Physics*, 143:104705, 2015.

[25] L. Chen, X. He, H. Liu, L. Qian, and S.H. Kim. Water adsorption on hydrophilic and hydrophobic surfaces of silicon. *Journal of Physical Chemistry C*, 122:11385–11391, 2018.

[26] M. Odelius, M. Bernasconi, and M. Parrinello. Two dimensional ice adsorbed on mica surface. *Physical Revue Letters*, 78:2855–2858, 1997.

[27] R Howland and L Benatar. A practical guide to scanning probe microscopy. thermomicroscopes, 2000.

[28] Ju-Ai Ruan and Bharat Bhushan. Atomic-scale friction measurements using friction force microscopy: part i—general principles and new measurement techniques. *Journal of tribology*, 116(2):378–388, 1994.

[29] John E Sader, Ian Larson, Paul Mulvaney, and Lee R White. Method for the calibration of atomic force microscope cantilevers. *Review of Scientific Instruments*, 66(7):3789–3798, 1995.

[30] William Tyrrell Thomson. *Theory of vibration with applications*. Pearson Education Limited, 2013.

[31] JP Cleveland, S Manne, D Bocek, and PK Hansma. A nondestructive method for determining the spring constant of cantilevers for scanning force microscopy. *Review of scientific instruments*, 64(2):403–405, 1993.

[32] H-J Butt, P Siedle, K Seifert, K Fendler, T Seeger, E Bamberg, AL Weisenhorn, K Goldie, and A Engel. Scan speed limit in atomic force microscopy. *Journal of microscopy*, 169(1):75–84, 1993.

[33] P. Timoshenko and J.N. Goodier. Theory of elasticity, 1970.

[34] DF Ogletree, Robert W Carpick, and Miguel Salmeron. Calibration of frictional forces in atomic force microscopy. *Review of Scientific Instruments*, 67(9):3298–3306, 1996.

[35] Huabin Wang and Michelle L Gee. Afm lateral force calibration for an integrated probe using a calibration grating. *Ultramicroscopy*, 136:193–200, 2014.

[36] Xing Ling, Hans-Jürgen Butt, and Michael Kappl. Quantitative measurement of friction between single microspheres by friction force microscopy. *Langmuir*, 23(16):8392–8399, 2007.

[37] M Varenberg, I Etsion, and G Halperin. An improved wedge calibration method for lateral force in atomic force microscopy. *Review of scientific instruments*, 74(7):3362–3367, 2003.

[38] Ewa Tocha, Holger Schönherr, and G Julius Vancso. Quantitative nanotribology by afm: a novel universal calibration platform. *Langmuir*, 22(5):2340–2350, 2006.

[39] KL Johnson. Adhesion and friction between a smooth elastic spherical asperity and a plane surface. *Proceedings of the Royal Society of London. Series A: Mathematical, Physical and Engineering Sciences*, 453(1956):163–179, 1997.

[40] Zinaida Kutelova, Hendrik Mainka, Katja Mader, Werner Hintz, and Jürgen Tomas. Glass spheres: Functionalization, surface modification and mechanical properties. In *Surface Effects in Solid Mechanics*, pages 95–104. Springer, 2013.

[41] JJ Cras, CA Rowe-Taitt, DA Nivens, and FS Ligler. Comparison of chemical cleaning methods of glass in preparation for silanization. *Biosensors and bioelectronics*, 14(8-9):683–688, 1999.

[42] Mario Castano-Alvarez, Diego F Pozo Ayuso, Miguel García Granda, M Teresa Fernández-Abedul, Jose Rodríguez García, and Agustín Costa-García. Critical points in the fabrication of microfluidic devices on glass substrates. *Sensors and Actuators B: Chemical*, 130(1):436–448, 2008.